© 2013 by Nitish Sanghi. All rights reserved.

DESIGN OF FLEXIBLE ACTUATORS USING ELECTRO-ACTIVE POLYMERS AND CPG-BASED CONTROL STRATEGIES

BY

NITISH SANGHI

THESIS

Submitted in partial fulfillment of the requirements
for the degree of Master of Science in Mechanical Engineering
in the Graduate College of the
University of Illinois at Urbana-Champaign, 2013

Urbana, Illinois

Advisor:

Assistant Professor Soon-Jo Chung

Abstract

Biomimetic design based on inspiration from nature for solutions for engineering problems has been practiced throughout human history. Invertebrate animals without a skeletal structure have flexible, robust and agile movements. For example, the octopus arm which is able to grip objects by exerting large forces, moves with a wide range of velocities, and manipulates delicate objects, without any rigid skeletal elements. Two key applications of such biomimetic systems are compliant and lightweight robotic arms for tightly constrained spaces and energy-efficient muscle actuators for biomimetic locomotion.

Inspired by octopus arm, in this thesis we investiagte different design concepts and requirements for using dielectric electroactive polymers (EAP) for designing of flexible actuators and manipulators. A model-guided approach to design a bio-inspired flexible actuator module is presented analyzed. Further, mathematical modelling for Central Pattern Generators (CPGs) is presented. The condition for phase synchronization of coupled single chain oscillators is derived and various techniques for pattern generation using oscillator network are studied. Finally, octopus based control using Central Pattern Generators (CPGs) is briefly discussed.

Acknowledgments

This thesis would not have been possible without the guidance and the help of several individuals who in one way or another contributed and extended their valuable assistance in preparation and completion of this thesis. This work was supported by U.S. Army Research Office (ARO) under Award No W911NF-10-1-0296. First and foremost, I would like to thank my adviser Professor Soon-Jo Chung for his guidance. I would also like to thank Dr. Michael McFarland and Prof. Ashraf Bastawros at Iowa State for their invaluable inputs and fellow graduate students Michael Dorothy and Jin Yu Guan, for their efforts and inputs.

To my parents

Table of Contents

List of Figures

Chapter 1

Introduction

The motivation for designing flexible manipulator is inspired by the flexible and robust movements of invertebrate animals without rigid skeletons such as cephalopods, annelids or arthropods. Octopus arms, elephant trunks, squid tentacles, for example, are able to grip objects by exerting large forces, move with a wide range of velocities, and have high flexibility as they can bend at any point and in any direction, as well as elongate, shorten, and twist, without any rigid skeletal elements. Octopus arms, as well as elephant trunks, squid tentacles, and vertebrate tongues are called muscular hydrostats, since they maintain a constant organ volume, thereby enabling a complex movement without skeletal support. They form a stiffened dynamic skeleton by co-activation of three groups of muscles including axial (longitudinal and transverse), oblique, and circular muscle stacks [54], as depicted in Figure 1.1.

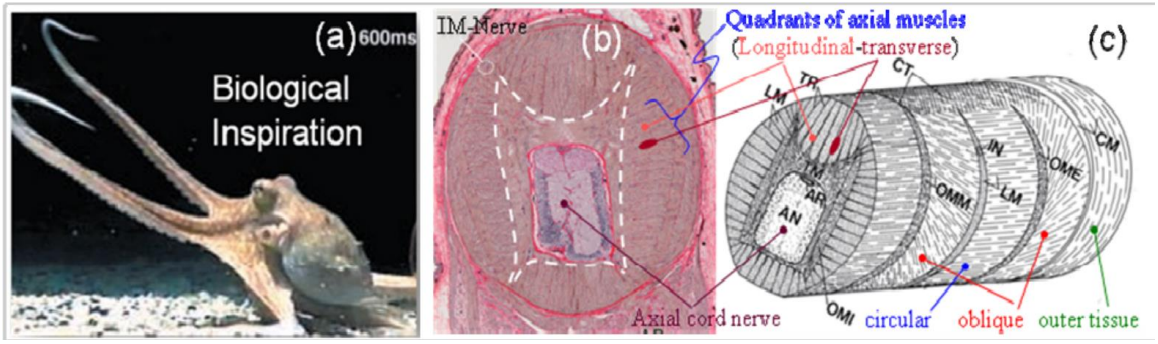

Figure 1.1: (a) Biological inspiration, octopus arm reaching via propagation of localized bend [31]. (b, c) Transverse section of octopus arm, showing the three groups of synergistic muscles and intramuscular sensory nerve [54].

The emergence of new materials that harness the coupling between the intrinsic mechanical deformations (strain energy) and the applied external field (electrical, electromagnetic, electrochemical, and/or electro-osmotic fields) has provided a new direction for miniaturized actuation and control (see Figure 1.2).

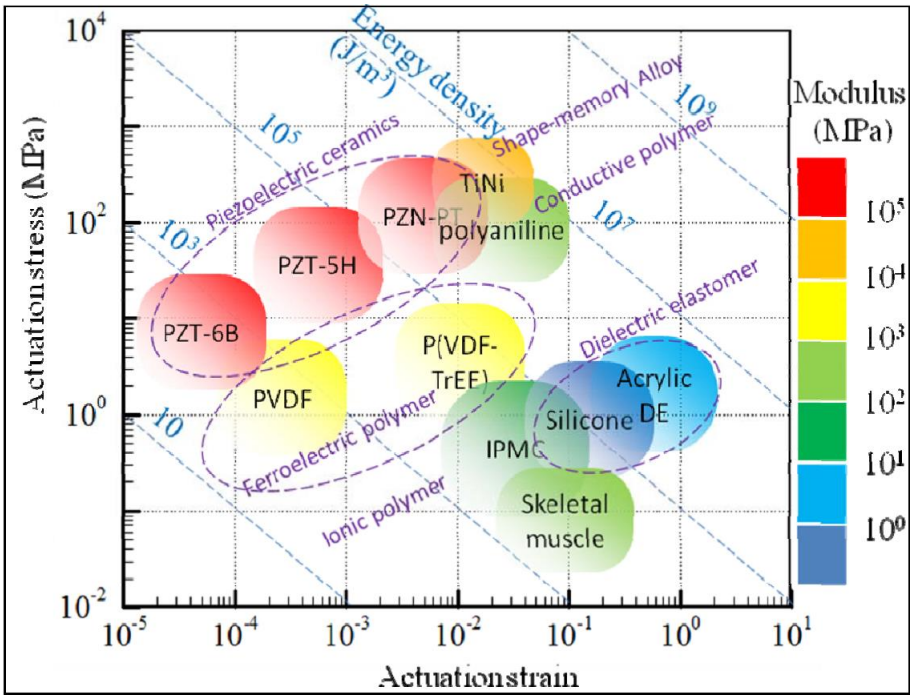

Figure 1.2: Common types of actuator materials and their limits of stress and strain. EAPs modulus span three order of magnitudes [1, 2]

A number of different hyper-redundant flexible structures that mimic muscular hydrostats like the octopus arm have been attempted, most notably by using pneumatic air muscles (PAM), shape-memory alloys (SMA), and piezoelectric ceramic (PZT) [26]. Various trade-offs govern the performance of this class of materials, ranging from power density and time response to force and stroke. Also, the small strains of the piezoceramics (0.1 percent) [6] and the low electromechanical coupling of the shape-memory alloys [9] limit their utilization for large-scale maneuverability. Electro-active polymer-based actuator materials are expected to work better than piezoelectric ceramic (PZT) actuators and shape-memory alloys (SMAs) since they are expected to provide power densities within a factor of 3-5 of the

electric motors but with the added flexibility of their muscle-like nature. Moreover, EAPs are a viable candidate for actuation as they exhibit quick response times and are capable of large strains (10-100 percent). Dielectric elastomers are commercially available in the form of tapes from 3M (VHB tapes). They are usually pre-strained on frames (up to 500 percent) to reduce the actuation voltage and increase breakdown voltages. Pre-straining causes there to be internal tensile stresses in the material during a non-activated state which can then be used for actuation when activated. Electro-active polymeric actuators primarily belong to two groups of materials - one group being electric EAPs in which the actuation is in response to the electric field; and the other group being ionic EAPs in which the presence and movement of ions in an electrolyte leads to the actuating behavior. In essence, ionic EAPs require low voltage but necessitate constant hydration, and produce low stress limiting their applications [14]. Significant work has been done to explore the potential of the EAPs in actuator technologies while attempting to model the behavior of this material. An attempt to mimic the functionality of a muscular hydrostat has been made by [36] et al. using electro-active polymers (EAPs). Different designs for a hyper-redundant robotic arm that utilizes dielectric electro-active polymers (DE EAPs) as artificial muscles have been explored such as out-of-plane actuation has been looked at and implemented using an agonist-antagonist configuration of the EAPs [52].

Recent advances in neurobiology have provided different lines of evidence which suggest that motor actions and movements in both vertebrates and invertebrates are composed of elementary building blocks, which are loosely referred to as motion primitives [18]. High-speed video analysis of an Octopus vulgari that grabs a target by reaching an arm [30, 51, 52] showed a wave-like propagation of a bend that travels from the base of the arm toward the tip via synergistic contraction of local transverse and longitudinal muscles [30]. In other words, reaching movements are composed of straight lines with bell-shaped velocity profiles. Similar bend propagation is seen in other octopus arm movements such as locomotion and grasping. The extracted kinematics data [18, 30] showed that the bend tends to move within

a single plane in a simple, slightly curved path connecting the center of the animals body with the target location. Approximately 70 percent of the reaching movements demonstrated a stereotyped tangential velocity profile. An invariant profile was observed when movements were normalized for velocity and distance. Two arms, when extended together in the same behavioral context, demonstrated identical velocity profiles [18]. The stereotyped features of the movements were also observed in spontaneous arm extensions (not toward an external target). The simple and stereotypic appearance of bend trajectories suggests that the position of the bend in space and time is the controlled variable. The utilization of such a vertebrate-like strategy, temporarily reconfiguring the arm into a stiffened, articulated, quasi-jointed structure by using motion primitives and distributed and hierarchical cell-based actuation in the proposed bio-inspired flexible structures will reduce the immense redundancy of the systems movements and hence simplify the complexity of sensing and control. The anatomy of an octopus arm reveals a highly localized sensory feedback system which is believed to be an important factor in realizing its unique arm movement based on stereotypical motions [22, 50]. The embedded receptor cells in the periphery of the muscle (Figure 1.1) sense a local stretch due to bending deformation. These intramuscular stretch receptors are connected to the axial nerve cord, which runs along the cross-sectional center of the octopus arm at intervals of approximately 200 μ m. Sumbre et al.[19] experimentally showed that octopus arms are capable of producing their typical motor activities even after the neural connections with the brain were severed, which corroborates the hypothesis of the localized nature of the stereotypical octopus arm motions. This corroborates our hierarchical distributed control strategy inspired by neural central pattern generators (CPGs) [13, 21, 28]. Furthermore, the implication of this localization to the proposed bio-inspired flexible actuating systems is the need for sensing schemes capable of registering the degree of local curvature as a semi-continuous or, preferably, a continuous function of location. The exact bio-mimetic solution, i.e., embedding a large number of sensors with a limited sensing range, will be increasingly inefficient as the bio-inspired flexible structure is increas-

ingly miniaturized. For efficient bio-mimetic implementations, the use of a neurobiologically inspired control scheme which utilizes information on the local curvature in a distributed or quasi-distributed fashion will be very beneficial. This thesis consolidates ideas for artificial muscles and their use for designing continuum/discrete, hyper-redundant manipulators and presents a number of design concepts for this using electroactive polymers material model. Also presented are design concepts for control of these biomimetic systems using Central Pattern Generators (CPGs).

1.1 Overview

The organization of the thesis is shown in Figure 1.3. Chapter 2 discusses the principle of DE EAP actuation and prototyped in literature. Chapter 3 presents some general remarks for using EAPs for actuator/ flexible manipulator design. Chapter 4 discusses design of various actuator/ artificial muscles are examined. Chapter 5 presents mathematical modeling of one actuator module and some design insight on their applications. Chapter 6 discusses concepts related to Central Pattern Generators (CPGs) based on Hopf Oscillators. In Chapter 7, control strategies using CPGs for control of hyper-redundant systems are discussed. Chapter 8 presents conclusions emerging from the thesis.

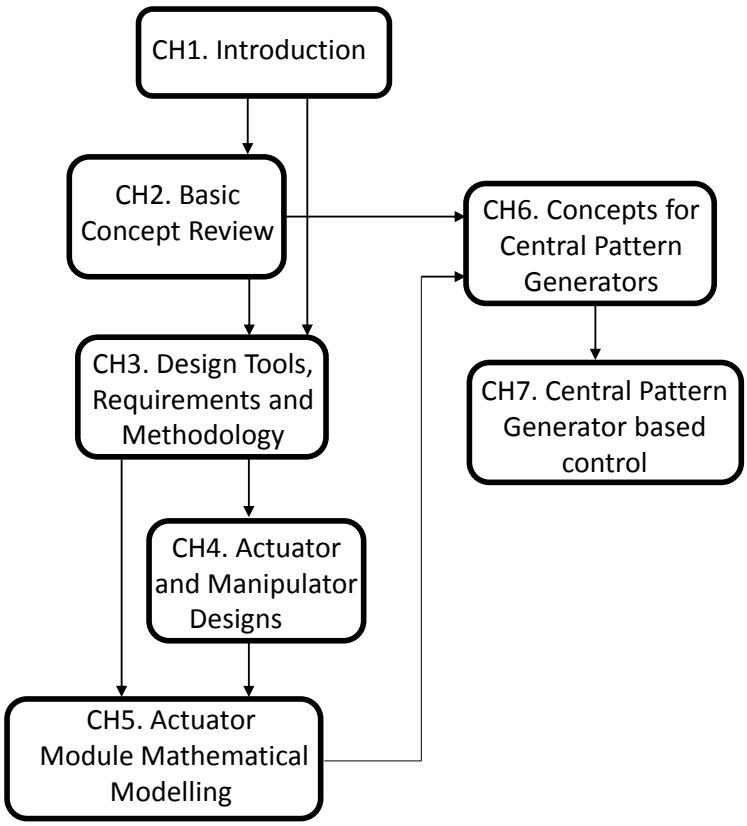

Figure 1.3: Organization of Thesis

Chapter 2

Basic Concept Review

2.1 Dielectric Electroactive Polymers (EAPs)

Polymers can deform under external stimulation. The external stimulation can be electrical, thermal, chemical, or magnetic [36]. For the purpose of this thesis, we are solely interested in the electroactive polymers. Dielectric Electroactive Polymers (DE EAPs) are electroactive polymers, in which a change in shape or volume is induced under stimulation by an electrical voltage. Essentially, DE EAPs consist of two compliant electrodes with a thin EAP film in the middle. For activation, a high DC voltage in the range of several kilovolts is applied across the compliant electrodes. Analogous to the working of a capacitor, one electrode gets a positive charge and the other a negative charge. The opposite charges across the film gives rise to electromechanical effects. The same charge on a side, also gives rise to electromechanical effects. The opposite charges on the electrodes attract and squeeze the DE EAP film in the thickness direction [36] and the incompressible DE EAP expands in the planar direction. Also, the same charge on each electrode creates repelling forces, which pulls the film in the planar direction.

As in Figure 2.1 [36], when the voltage $U = 0$ or the system is short circuited, the DE EAP is in deactivated state, the charge $Q = 0$ and thickness of DE EAP film is d^o. When activated by application of an electrical voltage $U > 0$, the charge becomes $Q > 0$ and the thickness of DE EAP reduces to d and the film expands as shown.

An important point to note is that actuator configurations depend on whether the DE EAP film is prestrained or not. The prestraining technique used for purpose of this thesis

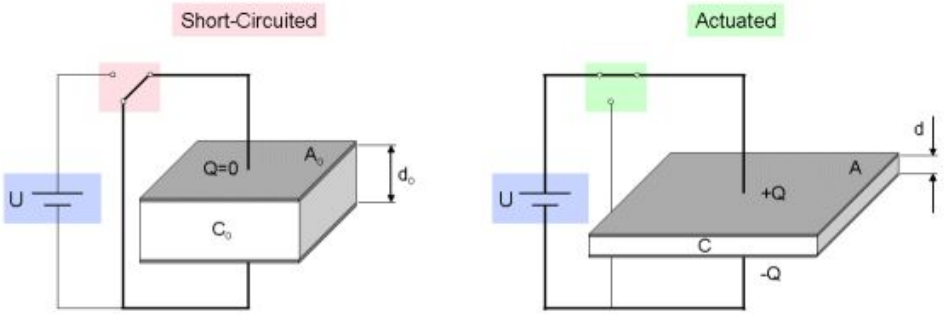

Figure 2.1: Working principle of Dielectric Electroactive Polymer [3]

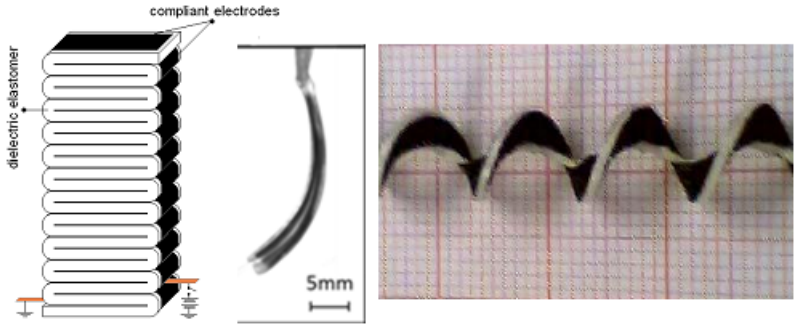

Figure 2.2: Actuators with unprestrained DE EAP: Folded Actuator [8], Uni-morph Actuator [35] and Helical Actuator [7] (Left to right)

is explained in the next chapter. Examples of actuator which do not have a prestrained DE EAP are shown in Figure 2.2. Figure 2.3 illustrates examples of actuator configurations requiring prestrained DE EAP.

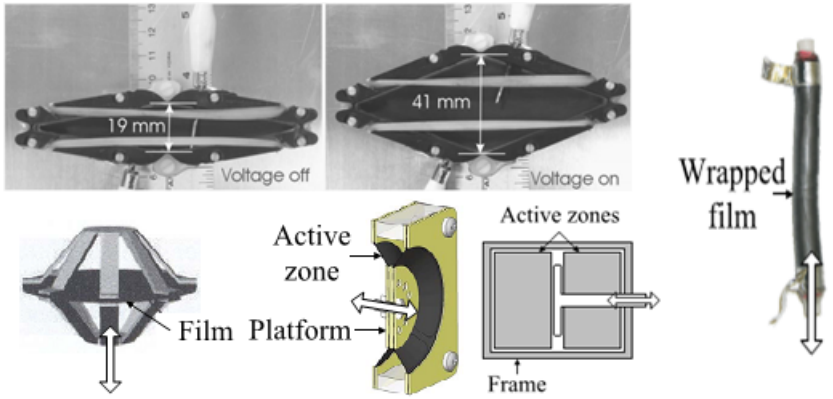

Figure 2.3: Actuators with prestrained DE EAP: Diamond Shaped Hinge Actuator [43] (top), Spider actuator, UM actuator, push-pull actuator and Spring Actuator [36]

These actuator designs can be used for a number of engineering applications. As an example relevant for this thesis, in Figure 2.4 are flexible manipulator designs. The design on the left is based on the spring roll actuator and the one on the right is based on the hinge design [36].

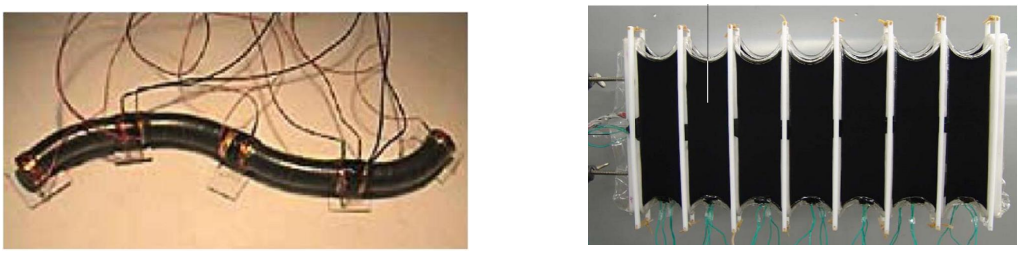

Figure 2.4: Examples of flexible manipulators designed and developed using DE EAP actuators: spring roll based manipulator, hinge based manipulator [36].

2.2 Central Pattern Generators

Central pattern generators (CPGs) are neural networks that can produce rhythmic patterned outputs without rhythmic sensory or central input. These networks are present in animals, both vertebrates and invertebrates. CPGs are constructed using nonlinear oscillators coupled together with parameters and coupling gains tuned to produce desired outputs. From a biological prospective, CPGs are known to relieve the computational burden of locomotion in the brain and to avoid issues of time-delay in feedback and learning by distributed local computation [10]. CPG based control has a number of advantages. Firstly, CPG-based control reduces the dimensionality and bandwidth of signals required from the main controller to the actuators [10] and secondly, the CPG parameters can be easily modulated to achieve different actuator control outputs [10].

Oscillator models like Matsuoka Oscillator [32], Hodgkins Huxley model [25], Mcmillen Neural oscillator [37], Hopf oscillator [11], Van Der Pol oscillator [29] and Rayleigh oscillator

[15] have been used for CPG network design. The first three are designed to mimic/simulate neurons and the latter three are more abstract representation. Van Der Pol and Rayleigh oscillator are briefly discussed below. For the purpose of this thesis we use the Hopf oscillator, which will be discussed in chapter 6.

2.2.1 Van Der Pol oscillator

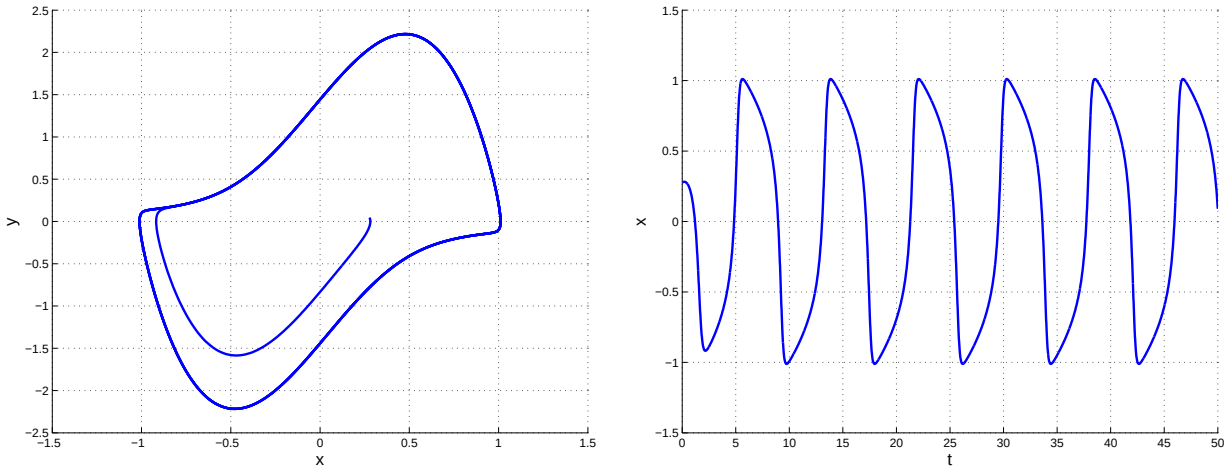

(a) Phase portrait (b) Output signal

Figure 2.5: MATLAB simulation for Van Der Pol oscillator: $\mu = 10, \rho = .25$ and $\omega = 1$

Van Der Pol oscillator have been extensively used for building CPG networks for control of bio-inpsired robots [4, 24]. In general form, the equation for VDP is as in Eqn. (2.1), where μ is the damping parameter, ρ is the amplitude and ω is the frequency. For $\mu = 0$, the equation reduces to that of a simple harmonic oscillator. And for $\mu > 0$, there exists a stable limit cycle which depends on the parameters. Due to lack of circular symmetry, it is not possible to exactly define a phase angle relation between two coupled VDP oscillators.

$$\ddot{x} - \mu(\rho^2 - x^2)\dot{x} + \omega^2 x = 0 \tag{2.1}$$

2-dimensional form of Eqn. (2.1) is :

$$\dot{x} = y, \quad \dot{y} = \mu(\rho^2 - x^2)y - \omega^2 x \tag{2.2}$$

2.2.2 Rayleigh Oscillator

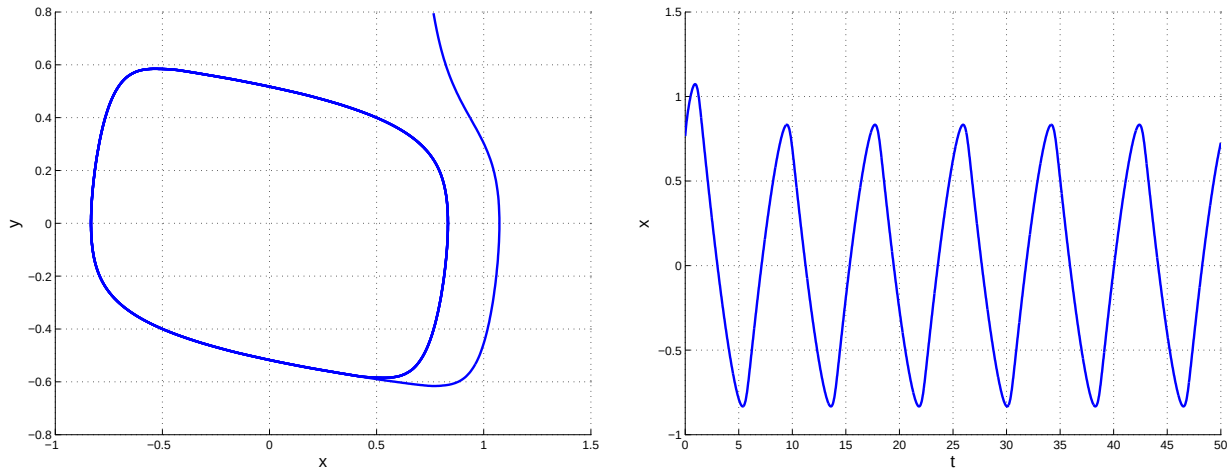

(a) Phase portrait (b) Output signal

Figure 2.6: MATLAB simulation for Rayleigh oscillator: $\mu = 10$, $\rho = .25$ and $\omega = 1$

Rayleigh oscillator is similar to VDP oscillator and has also been used for building CPG networks for control [16, 38, 39]. In general form, the equation for Rayleigh oscillator is as in Eqn. (2.3), where μ is the damping parameter, ρ is the amplitude and ω is the frequency. For $\mu = 0$, the equation reduces to that of a simple harmonic oscillator. And for $\mu > 0$, there exists a stable limit cycle which depends on the parameters.

$$\ddot{x} - \mu(\rho^2 - \dot{x}^2)\dot{x} + \omega^2 x = 0 \tag{2.3}$$

2-dimensional form of Eqn. (2.3) is :

$$\dot{x} = y, \quad \dot{y} = \mu(\rho^2 - \dot{x}^2)y - \omega^2 x \tag{2.4}$$

2.2.3 Network Topology

Network topology is the arrangement of the various elements oscillator/biological network. CPGs network topology plays an important role and has a great deal of influence on the dynamics of the network. Coupling between oscillators will affect the frequency, the phase, and the amplitude. A few examples of coupled oscillator network topologies are illustrated in Figure 2.7. The network topologies can be represented by a laplacian matrix L. Laplacian

(a) Single Chain Network (b) Ring Network

Figure 2.7: Coupled Oscillator Networks [11, 12, 46]

matrix is constructed using adjacency A and degree D matrices [20] using the relation, $L = D - A$. The degree matrix is a diagonal matrix which contains information about the number of incident edges of each oscillator in the network. The adjacency matrix represents, which oscillators of the network are adjacent to which other oscillator. The laplacian matrix will be used in chapter 6 to analyze the stability of a single chain coupled oscillator network. In Table 2.1 shows the laplacian matrix L_1 constructed for the network in Figure 2.7a and L_2 constructed for the network in Figure 2.7b.

$$L_1 = \begin{pmatrix} I_2 & -I_2 & 0 & 0 \\ -I_2 & 2I_2 & -I_2 & 0 \\ 0 & -I_2 & 2I_2 & -I_2 \\ 0 & 0 & -I_2 & I_2 \end{pmatrix} \quad L_2 = \begin{pmatrix} 2I_2 & -I_2 & 0 & 0 & -I_2 \\ -I_2 & 2I_2 & -I_2 & 0 & 0 \\ 0 & -I_2 & 2I_2 & -I_2 & 0 \\ 0 & 0 & -I_2 & 2I_2 & -I_2 \\ -I_2 & 0 & 0 & -I_2 & 2I_2 \end{pmatrix}$$

Table 2.1: Laplacian matrix constructed for the network topologies in Figure 2.7.

Chapter 3

Dielectric EAP Actuator Design Methodology

For the design and development of DE EAP based actuators and flexible manipulators, it is important to understand the characteristics of the material. In this chapter, we discuss the material properties which have been stated in literature and some further tested for the purpose of this thesis. The initial process used for fabricating DE EAP actuators is discussed. During the fabrication process, it is important to carefully handle the DE EAP film material and electrode material; these issues will be addressed in the following sections. We begin the discussion with prestraining the DE EAP and the process we used for prestraining the DE EAP. The mathematical model used for the purpose of this thesis is discussed in some detail. Electrodes are an important component of DE EAP actuators, thus we discuss electrode materials and application process used in detail. Further, we discuss concept of support structure and how it was used and designed. Finally, some ideas for switching system are presented.

3.1 Remarks for Design of Actuators

The DE EAP actuators designed and fabricated have different components, and due care needs to be taken while designing and fabricating them. The DE EAP film, electrode material, support structure, the core and the wiring are the main components of the DE actuators. Based on experience, we conclude some technicalities, which need to be kept in mind while designing and fabricating the DE EAP actuators. In this section, we elaborate on them.

3.1.1 Prestraining the EAP

For a stress free Dielectric EAP film, interpenetrating network (IPN) process can be used for pre-straining. The actuators fabricated using IPN process do not require any support structure to maintain the pre-strain. The only drawback of using IPN process is that it requires special laboratory equipment and also is very time consuming. For pre-straining, a mechanical process can also be used. The mechanically pre-strained Dielectric EAP requires a support structure to which dielectric EAP needs to be attached and hence the flexibility in actuator module design and flexible manipulator design is constrained.

Dielectric EAP actuators were made using VHB 4910. VHB 4910 is manufactured by 3M, and is an acrylic material. It has a thickness of 1 mm. It was pre-strained in the planar directions using a pre-strainer. Pre-straining of the DE EAP film reduces the activation voltage and increases the breakdown strength. To quantify the pre-strain in the DE EAP film, we used the convention described in [36]. Pre-strain ratios are defined in the planar directions in terms of the initial lengths L_k^i and pre-strained final lengths L_k^f where $k = x, y$ by:

$$\lambda_k^f = \frac{L_k^f}{L_k^i} \tag{3.1}$$

DE EAP film can be pre-strained uniaxially or biaxially in the planar direction. Dielectric EAP can be prestrained in two ways.

3.1.2 Uniaxial Prestraining

In uniaxial pre-straining, length along only one planar direction is pre-strained. So, if pre-strained along x direction, then stresses σ_z^f and σ_y^f are zero, thus $\lambda_y^f = \lambda_z^f$. Eqn. (3.2) gives the relationship between prestrain and thickness in z direction.

$$L_z^f = \frac{L_z^i}{\sqrt{\lambda_x^f}} \tag{3.2}$$

3.1.3 Biaxial Prestraining

In biaxial pre-straining, the length along both planar direction is pre-strained. So, if pre-strained along x and y directions, then stresses σ_z^f is zero. Eqn. (3.3) gives the relationship between prestrain and thickness in z direction.

$$L_z^f = \frac{L_z^i}{\lambda_x^f \lambda_y^f} \tag{3.3}$$

Performance of biaxially prestrained dielectric EAP is better compared to uniaxially pre-strained. Maintaining this prestrain is not possible for all actuator modules. As can be seen in uniaxial tests by [23], if all sides of the dielectric EAP film are not attached to a support structure, then the free edge experiences a necking phenomenon which leads to a decrease in the prestrain in the necking direction. Furthermore, free edges are prone to ripping as there may be micro-abrasions that are left by the fabrication process. These edge problems significantly reduce the durability of the actuator, and care must be taken during the fabrication process to ensure that the abrasions are minimized. Activation voltage reduces because the electrode pressure which squeezes the DE EAP film in the thickness direction is proportional to the square of the applied electric field. Therefore, as the DE EAP film is pre-strained, the thickness reduces and so does the activation voltage. There is an increase in the dielelectric breakdown strength when pre-strained according to investigations of [33].

Prestrain Process

The DE EAP film has to be pre-strained for use in some design concepts. To pre-strain the film, a hand operated pre-strainer was designed and fabricated as seen in Figure 3.1. The pre-strainer can uniaxially or bi-axially pre-strain the film. For transferring the pre-strained film, we developed a process. Pre-strain frames were used. These frames were essentially rectangular frames of different dimensions according to requirements, fabricated using the CNC machine. The pre-strain frames had sufficient thickness to maintain the pre-strain

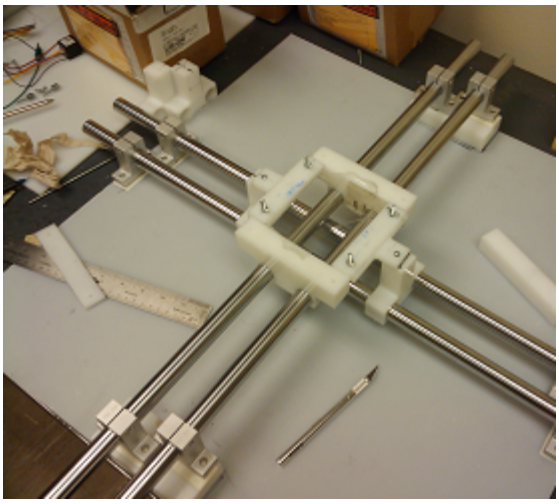

Figure 3.1: Prestrainer fabricated in the lab for the purpose of prestraining both biaxially and uniaxially

of the film until it was attached to the support structure of the actuator modules. HDPE was used for fabricating the pre-strain frames. Upon pre-straining the DE EAP film, the pre-strain frame was attached to the stretched film (Figure 3.2b). The pre-strain frame had a very thin double sided tape on its surface to secure the film onto the frame. The frame with the DE EAP film attached to it was then cut out using an Exacto knife.

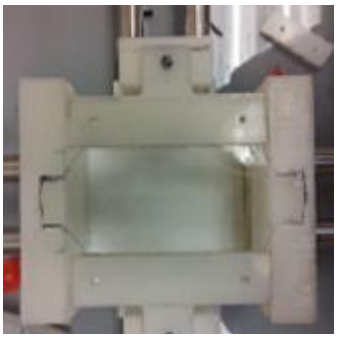

(a) Prestrained DE EAP film

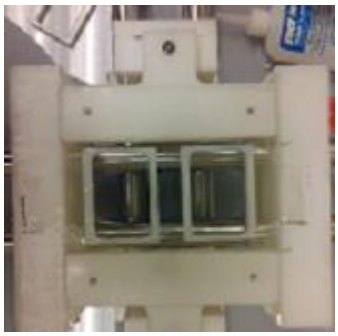

(b) Frames attached to DE EAP film

Figure 3.2: Prestrainer in use to prestrain DE EAP and transferring prestrained DE EAP onto pre-strain frames

3.1.4 Electrode Material Application and Selection

Different electrode materials were tested for use to fabricate the DE actuators. Criterea used were, ease of application and handling, performance, and response time. The electrodes were applied using a brush or blade or sprayed on using an air brush onto the prestrained EAP. Electrode materials used were carbon black powder, graphite powder and carbon grease. The electrodes materials can be categorized as dry electrodes or wet electrodes. Carbon black powder and graphite powder are dry electrodes whereas carbon grease is a wet electrode. In the beginning, carbon black and graphite based dry electrodes were brushed to the surface of the film of prestrained EAP. This process was fast and easy to implement. The drawback was that the electrode deposition on the surface of prestrained EAP was not uniform and depended heavily on the brush strokes and skills of the person. Locations with a dense amount of electrode material caused stress concentrations when activating the EAP which may have caused the elastomer to rip. Figure 3.3a illustrates a sample of DE EAP film with electrode deposited by brush. Also, since we were handling dry powder the particles would

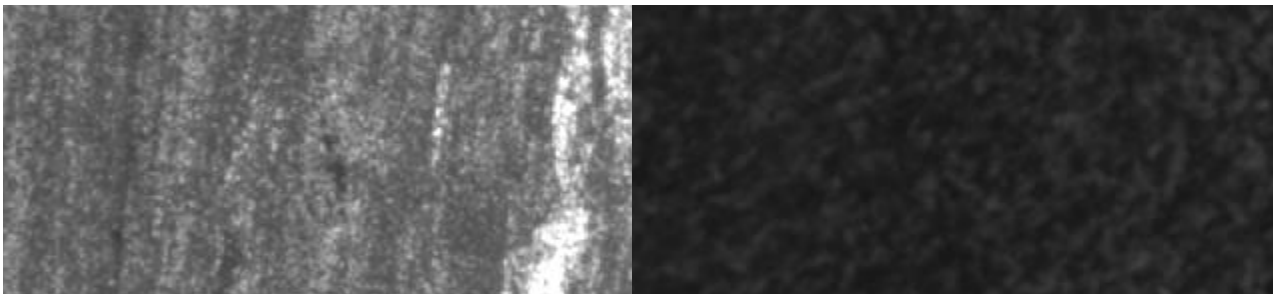

(a) Magnified surface image DE EAP with brushed electrode

(b) Magnified surface image DE EAP with air brushed electrode

Figure 3.3: DE EAP surface under microscope

float around. If the brushing speed was too fast, these particles would stick to DE EAP surfaces, where there was potential for a short circuit. To take care of these issues, propyl alcohol was used as a suspension medium for the dry powder particles. The two powders form a semi-liquid slurry in propyl-alcohol, and then it becomes easy to apply them as an electrode. Figure 3.3b illustrates a sample of DE EAP film with electrode deposited by air

brush. For applying carbon black, a brush was used, whereas for the graphite, an air brush was used. An air brush could not be used for the carbon black solution, because it choked the nozzle because of formation of aggregates of carbon black particles. Further, it was noticed that because carbon black particles are extremely small and form a very thin layer of electrode. Graphite particles form a thick layer. Also, for fabrication of multi-layered DE actuators, it became necessary to remove extra electrode material by scrapping it off. Otherwise air pockets form, and inadequate actuation occurs. The role of the electrodes on both sides of the EAP is to effectively squeeze the EAP in the thickness direction so that the material extends in the other two directions. Therefore, the electrode material must allow the elastomer to stretch and cannot be rigid. Furthermore, the area of the electrode should cover a maximum amount of area, however, a small inactive zone was left out at the edges or between adjacent electrodes to avoid arcing/short circuiting from one electrode to the other.

3.1.5 Breakdown of EAP Film

The prestraining was done for two reasons. One of them is to increase the breakdown voltage so that maximum performance is obtained. Thus, it is desirable to actuate the EAPs at a voltage level that is just below the dielectric breakdown strength of the material. Cyclic actuation at high voltages degrades the elastomer material and if the EAPs were operated at the breakdown strength, the material would fail after a few activation cycles. Physical damage to the EAP is done if the EAP fails due to dielectric breakdown, and a new EAP needs to be manufactured. The dielectric film which is essentially an insulator becomes conductive in the region of breakdown and short circuiting occurs. This way the material is fully utilized and can be used to produce the maximum deflection in actuator modules.

3.1.6 Core Material and Support Structure

As mentioned earlier, for actuator designs in which the EAP is mechanically prestrained, the agonist-antagonist configuration of actuators requires a core and support structure. This places a few constraints on the core and the support structure. If the a flexible core material is used to make the actuator like a gluestick, the core material must have the ability to resist the axial compression due to prestrain and simultaneously be as flexible as possible so as not resist the deflection and strain of the EAP actuators. It also needs to be able to maintain its own weight and at that of the support structure. An important point here is that the ability to resist axial compression decreases as flexibility increases. It is important to note that any decrease in prestrain or flexibility of a core will result in a reduction in performance of the arm as far as how much deflection and force is produced. The support structure needs to be rigid enough to resist deformation due to the prestrain but light enough so as to not add weight to the actuator. Also, it needs to cost effective and easy to handle during fabrication. We used PMMA and HDPE primarily. Some actuators, e.g. spring rolled, were also fabricated to test the concepts. Core material can also act like a support structure, e.g. the flexible muscle actuator discussed in a later section. An actuator design based on this concept was fabricated and concept testing was conducted.

3.2 EAP Modelling

In literature, a number of works are available to model and simulate the electromechanical deformation behavior of DE EAP film actuators when activated [34, 36]. Models incorporating linear material models have been used for describing dielectric films, but since DE EAP film has viscoelastic behavior, when used for fabricating actuators with large deformations occur, these models are not applicable. Hence, for defining the constitutive equations for the material we use the quasi static visco elastic model developed by Lochmatter et al. as in Eqn. (3.4). This model is more appropriate to describe the mechanical behavior of soft

polymer films. In this model, as the DE EAP film is incompressible ($\lambda_x\lambda_y\lambda_z = 1$), the overall effect of the electrodes is described by equivalent electrode pressure, $p_{\text{equivalent}}$, as in Eqn. (3.5) according to [41].

$$\sigma_i = K\lambda_i(\lambda_i - 1) - p \tag{3.4}$$

$$p = K\frac{1}{\lambda_x\lambda_y}(\frac{1}{\lambda_x\lambda_y} - 1) + p_{\text{eq}} \tag{3.5}$$

$$p_{\text{eq}} = K\epsilon_o\epsilon_r(\frac{V}{L_z})^2 = K\frac{\epsilon_o\epsilon_r}{\lambda_z^2}(\frac{V}{L_z^{(o)}})^2 \tag{3.6}$$

In Eqn. (3.4), σ_i is the stress in planar directions, K is a material constant, and λ_i is the prestrain in "ith" direction. The stress in the prependicular direction is defined by Eqns. (3.5) and (3.6), where p_{eq} is the maxwell pressure, ϵ_i are the constants of permittivity, V is the voltage applied across the DE EAP film, and L_z is the thickness of the DE EAP film. As mentioned in the section 3.1.6, for designs with core structure, the DE EAP film will be attached to a surface, hence, we need to know the force that the film exerts on the structure. For this, we assume that the film has constant cross sectional area A as shown in Figure 3.4. The force per unit width exerted by the DE EAP film is as in Eqn. (3.7), where $\frac{A}{W}$ can be

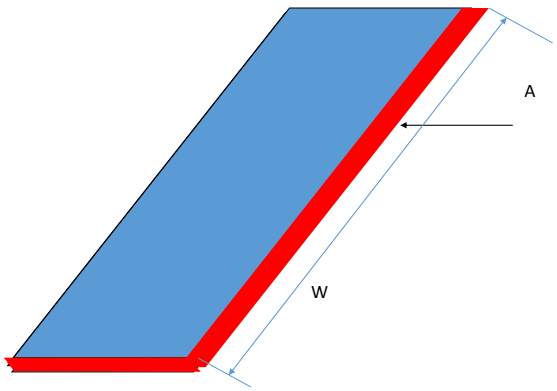

Figure 3.4: Prestrained DE EAP cross sectional area for force determination

replaced by $\frac{L_z^o}{\lambda_i\lambda_j}$.

$$F = N_{\text{layers}}\sigma_x\frac{A}{W} = N_{\text{layers}}\frac{A}{W}K\lambda_i(\lambda_i - 1) - p \tag{3.7}$$

In Eqn. (3.7) A is the cross sectional area of the DE EAP film in the direction prependicular

to the plane, N_{layers} is the total number of film layers, and W is the dimension of the film, along which the film is attached to the support structure.

3.3 Switching

DC high voltages in the range of a few kilovolts and supply current in the range of few microamperes are required for activation of dielectric EAPs. Commercially components are not available off the shelf for these diverging requirements of high voltages and low currents and the ones which may be available are very expensive. The system to control and operate a dielectric EAP actuator is made up of a power source, a control system, a sensing system for the actuator and a sensing system to monitor the high voltages and low current. Also, safety of operator needs to be kept in mind as the voltages are going to be in kilovolts but currents are in microamperes. To control the actuator the voltage characterization of the EAP has to be used which will be complemented by the actuator sensing system. Also, a sensing system is required for the power source to be able to accurately determine voltage and current levels as different components of the whole system will be operating at different voltage and current levels.

The power source system and the actuators have switches in between which are controlled by the control system. To supply the high DC voltage boost converters are being used. High voltage amplifiers are not being used because of safety reasons. A boost converter merely amplifies the voltage and reduces the current. $Q80$ series Emco boost converters are being used which have maximum voltage amplification to 8000 volts. The actuator while active may require different voltages for different segments hence more than one boost converter is required. There are various schemes that we can use to power the actuator depending on the number of boost converters used. Also, multiple number of boost converters are required as the using one single boost converter different EAPs cannot be activated at once. There is idle time, Δt, between activations, during which each segment is disconnected from the

source leads to an electrical self-discharging of the DE actuators. The idle time is mainly depends on the switching time and the voltage supply scheme being used. The switching time exits because of the mechanical nature of switches which in this case are reed relays. The characteristic charging time is given by $T = RC$ where R is the resistance of the whole circuit and C the capacitance.

Another aspect that requires to be considered is the discharging of the EAPs. The discharged energy needs to be absorbed either internally or externally in the actuator. In the internal absorption of energy there will be a short circuit circuit and in the external absorption the energy will be absorbed by the power source.

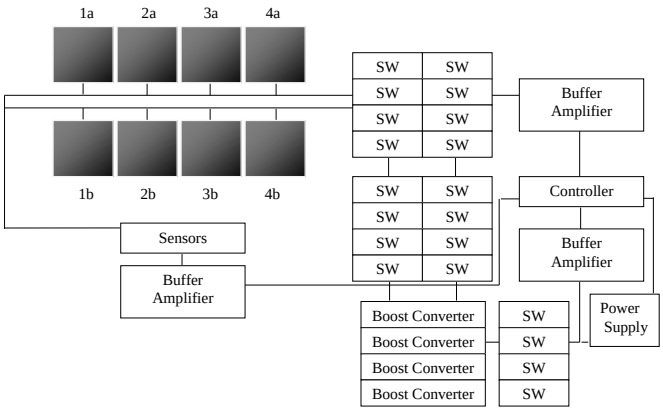

Figure 3.5: Switching system concept 1

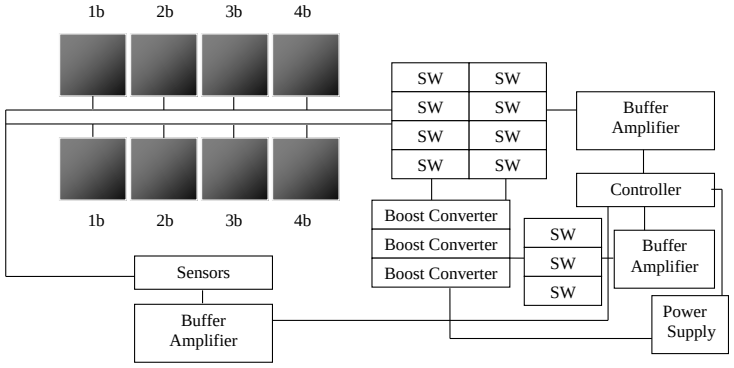

Figure 3.6: Switching system concept 2

In the schematics the EAP segments are numbered from 1-4. “a” and “b” represent two

films of EAP which are opposite to each other in a segment. When film "a" is actuated then film "b" contracts under tension, and thus bending the actuator. The switches are represented by SW. In Figure 3.5 there are 4 active segments with each segment composed of two opposite EAPs. Each EAP has a switch (SW) to control charging. There are four boost converters with each boost converter connected to all the EAPs. The controller operates at low voltages and the rest of the circuit at high hence we put in buffer amplifiers which allow only one sided connection and protect the controller from voltage surges. Now while being actuated different EAPs may require different voltages so the four boost converter can be set at different voltages at any one time and then the required switches can be turned on and off. In Figure 3.6 there are 4 active segments with each segment composed of two opposite EAPs. Each EAP has a switch (SW) to control charging. There are three boost converters with each boost converter connected to two adjacent EAPs. Each set of EAP has 2 boost converters connected to it. As two EAPs share one boost converter so when one EAP is not active then the other can use that boost converter and if the first EAP requires the boost converter then it can use the other boost converter.

3.4 Concluding Remarks

This material is still limited by various challenges. There is no established database or standard test procedure. Low actuation force, mechanical energy density and conversion efficiency are few mechanical challenges. The DE EAP is limited by the need for quite high voltage. Also, robustness issues like lifetime and reliability issues exist. It is not obvious how to make very large or very small EAP. There is a need for niche applications where it would not need to compete with existing technology.

Chapter 4

EAP Actuator Design

Conventional mechanical systems are driven by actuators which require components such as cams, gears, bushings, bearing, and other complex parts that are quite expensive and prone to failure. Thus, when compliant flexible mechanical systems need to be designed there is a dilemma. With the capability to mimic muscles, electro-active polymers (EAPs) have emerged as potential materials that can be used to actuate biologically inspired mechanisms. EAPs are resilient, fracture tolerant, noiseless actuators that consume low power and can be made miniature, low mass and inexpensive. EAPs can potentially be used to construct 3-D systems. The objective of this research work was to investigate and then design a bio-inspired octopus like flexible, hyper-redundant manipulator using EAPs. A number of different EAPs are available today with different actuation properties, and therefore selection can be made as required. Dielectric EAPs have been used most extensively because of their ease of use and cost effectiveness. Dielectric elastomers offer a wide variety of potential applications as a novel actuator technology that can replace many electromagnetic actuators, pneumatics, and piezo actuators. Dielectric elastomers can enable actuators to be integrated into applications that were previously infeasible, such as haptic feedback, pumps, prosthetics, and many more.

To design a flexible hyper-redundant, there are two primary methods. The first Method involves designing actuator modules that can be put together to fabricate flexible manipulators. In the second method, the manipulator are designed as a whole system without use of independent modules. Here, we have primarily used the module approach. In order to use dielectric EAP for the modules, it has to be prestrained so as to improve electromechanical properties and performance of the actuator modules. The agonist-antagonist configuration

based actuators are primarily designed and studied. Agonist-antagonist configuration is when two actuators are opposite of each other with a flexion region in between the two actuators like a biceps-triceps system in a human arm. When neither EAP is activated, the configuration is in equilibrium. The internal stresses in the prestrained EAP film are finite for σ_x and σ_y, while $\sigma_z = 0$. Upon activation of either EAP film, the film expands and σ_x and σ_y decrease and σ_z becomes nonzero because of the Maxwell pressure as stated in the previuos chapter. The DE EAP film on the other side is not activated and it contracts because of the force imbalance in the system due to the decrease in σ_x in the opposing EAP. The configuration is no longer in equilibrium, and the system deflects, a certain angle. The deflection and the force by which the non-activated EAP pulls with are highly dependent on the prestrain. Ideally, prestrain should be as large as possible. An increase in prestrain has many advantageous effects. It decreases the thickness of the EAP, and therefore decreases the activation voltage needed to make the EAP strain. More importantly for a robotic arm, it also increases the force generated by the actuator and the deflection of the arm. The VHB4910 elastomer material has inherent limitations in this area. Obviously, there is a limit to how much prestrain is possible before the material rips. But the force generated by the EAP is proportional to its size and prestrain. Therefore, it is desirable to have a large actuator. However, large actuators require large attachment points to maintain the prestrain which results in a large structure. The manipulators must be as lightweight as possible to ensure that minimum amount of force generated by the EAP is used to support the weight of the structure. Furthermore, there is an optimum size for the manipulators that provide maximum force or moment output.

4.1 Flexible Manipulator and Actuator Module Designs

For designing flexible manipulators, different design concepts were investigated. A few were fabricated in the lab, and others were simulated in MATLAB to determine feasibility. The design concepts explored were either based on actuator modules or full length manipulator fabrication. The fabricated designs were actuated to determine how well the actuator design works by measuring the deflection observed. The prestrain on the Dielectric EAP film was set at 3x5 with actuation in the direction of lower prestrain. This was done because of experience from earlier testing of material and recommendations in current literature. In this chapter we discuss the design procedure and methodology for the different design concepts fabricated and tested. In the next chapter mathematical models will be discussed.

4.2 Link Rotation based Design Concept

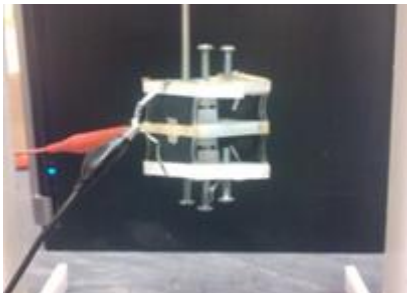

(a) Fabricated 2 segement ball joint actuator module

(b) Ball joint actuator module connected to testing setup

Figure 4.1: Fabrication and testing of 2 segment ball joint actuator module

This actuator module design concept is based on the agonist-antagonist configuration of DE EAPs. Each module consists of frames that can have rectangular or square shape. The two frames are connected using rotatory joints. Depending on the number of degrees of freedom in the module design, we either use a pin joint (1 degree of freedom) or a ball joint

(2 degrees of freedom). The dimensions of the frames decide whether one or more joints are required. The joint distance can vary depending on the module design requirements. A preliminary study was done in [36] for simple design. The pre-strained DE film is attached on the edge of the frames. For the design with one degree of freedom DE films are attached only on opposite sides and for the design with 2 degrees of freedom, on all sides of the frames. It is important that the weight of the module is minimal for acceptable performance of DE EAPs. The frames made up of light-weight high-density polyethylene (HDPE) have sufficient structural rigidity to resist deformation due to prestrain forces of the DE EAP film. And because, the EAPs are driven electrically, the non-conductivity of the HDPE prevents any undesired charge from transfering from one DE EAP film to another DE EAP film.

Figure 4.2: Prestrained DE EAP attached and electrode deposited onto film.

Several modules were fabricated and tested. These modules had square frames (for more dimensional details see appendix). They were fabricated using a CNC machine. A ball and socket joint was used. The DE EAPs were mounted on the edges using the pre-strain frames. Electrical contacts are used which are made up of aluminium. Total deflection of about 3-5 degrees is observed at voltages just below breakdown voltage. Dielectric breakdown occurs if EAPs were activated on one side for substantial time. The small deflection observed was primarily due to bowing of the free edges that reduces the prestrain in the DE EAP films. Also, the module had only one layer of DE EAP film which had to overcome forces due to the weight of the frames and friction in the ball joint. To counter the free edges, strips of prestrained EAP film were attached (as shown in Figure 4.1b) to reduce bowing-in.

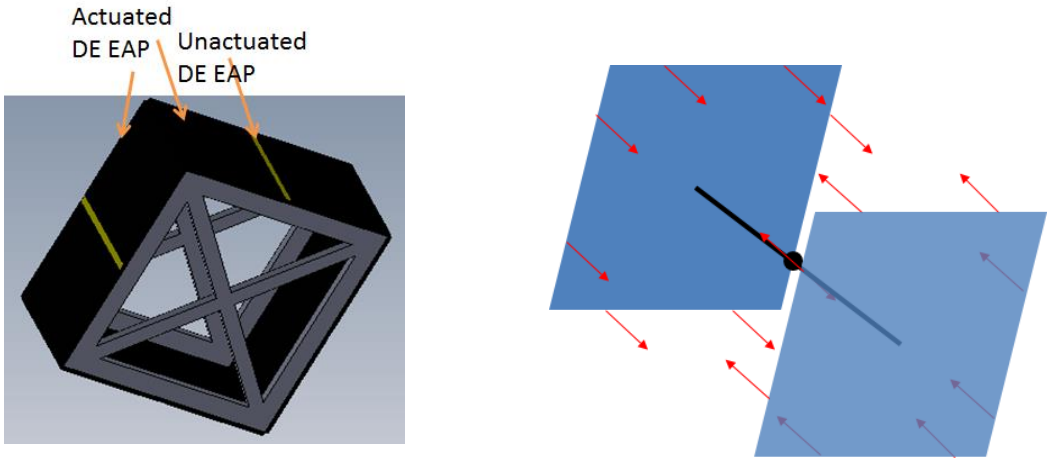

(a) CAD Design Concept (b) Independent force vectors in the module

Figure 4.3: 2 DOF per side actuator

No significant improvement was observed, however, bowing in reduced significantly. These modules can be connected in series to form a discrete flexible manipulator. Variations of this design include tapered modules and discretized electrode on DE film. These are further discussed in following sections.

4.3 Flexible Muscle Design Concept

The flexible muscle design is based on the agonist-antagonist configuration. Here, the core is also the support structure. The advantages of such a configuration are reduction in weight and fewer components required. Also, the actuator module is highly flexible. A number of different materials can be used for the core. The EAP muscle is entirely made up of EAP material itself and thus it is very flexible and light weight. The muscle has a 2 inches long and 2 mm thick layer of unprestrained EAP as its core with pre-strained (3x5 prestrain) layers of EAP attached on opposite surfaces of the EAP core (Figures 4.4a and 4.4b). Just like the ball joint segment design, the active EAP layers on the core are opposite to each other and also in tension. When one active EAP layer is activated, it relaxes, and the other

contracts, and the whole muscle segment bends. The deflection is continuous, as can be seen in Figure 4.4c. Deflections of up to 30 degrees have been observed Figure 4.4c. The EAP muscle actuators with more number of layers of active EAP have higher deflection, but as the number of layers increases so does the mass of the muscle which counteracts the movement observed. Note that the muscle has only one dimensional motion. This design concept has the potential to be extended to a full arm that has planar movement as shown in Figure 4.5.

(a) Actuator CAD concept (b) Fabricated Actuator (c) Actuator in activated state

Figure 4.4: Flexible Muscle Actuator

4.4 Flexible Core Design Concept

The EAP core design is based on the EAP muscle segments. It is equivalent to a number of EAP muscles put in series together. An unprestrained EAP layer of 2 mm thickness and 10 inch length is layered with active EAP segments in opposite surfaces. The EAP is a soft polymer and therefore very flexible. The core needs to support the axial load due to the prestrained EAP layers, which it is able to with EAP core but not as good as was expected. Also EAP film has a low modulus and thus it is not able to support its own weight. It bends significantly under gravity and is not able to counter act gravitational force when a active EAP layer is activated. Therefore, the core needs to be stiff enough to support its own weight and flexible enough to bend when activated. The fabricated EAP core design

did not work as expected. The EAP core was not stiff enough to support its own weight and also the axial loading due to the prestrained EAP films. The EAP muscle on the other hand was able to do so. Another problem was that if we make the EAP core thicker to increase stiffness then it becomes too bulky to support its own weight.

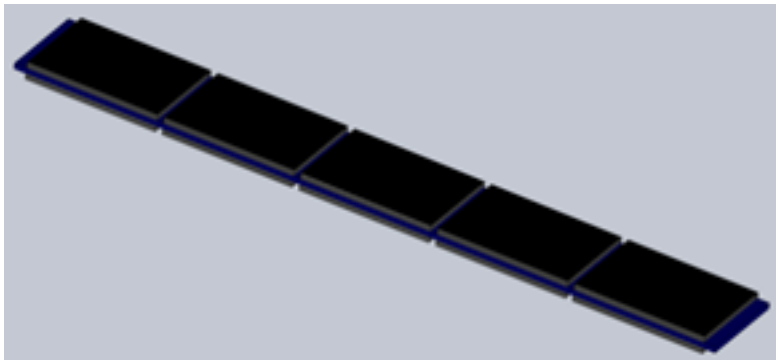

Figure 4.5: Flexible Core Design with DE EAP core

Another design concept utilized a flexible core material to facilitate bending of the arm as opposed to using ball joints. This design allowed the arm to bend at any point whereas the ball joint design only allowed the arm to bend at specific points along the arm. The flexible core was made out of glue stick material. Circular structural rings were then situated along the length of the core. In this design, the EAP was to be first prestrained, electroded in a specific pattern, and then rolled onto the structural rings. The rolling process has been used in previous EAP actuator designs such as the spring roll actuator. This design removed any free edges and was supposed to decrease the necking problem that reduces prestrain. Figure 4.6b shows the flexible core and the structural rings along the length. The process of rolling the prestrained EAP onto the rings required many attempts. Upon successfully doing so (and even though there were no free edges in the design), the EAP bowed inward (towards the core) in-between the structural rings. This was because the rings were too far apart. A solution to this was to significantly increase the number of rings on the core, but this turned out to be an impractical solution. Increasing the number of rings on the core decreased the length of the flexible core between any two rings and resulted in a higher bending stiffness.

The portion in between two rings became too stiff for the EAPs to bend. The biggest obstacle to overcome for this design was finding a sufficiently flexible core material that would allow the EAP to bend it but also be stiff enough to maintain the prestrain of the EAPs.

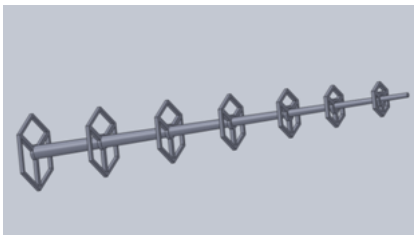

(a) Glue Resin Tapered Core Design

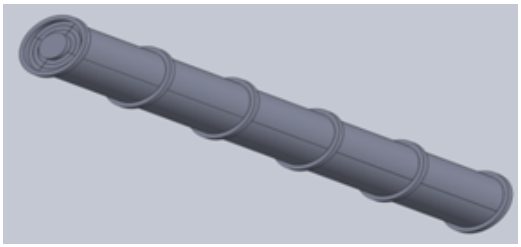

(b) Flexible Core Design with glue resin core

Figure 4.6: Flexible Core Designs

4.5 Sphere Core Design Concept

In this design, small sphere core was used. The core is made up of spherical beads aligned in a straight line and wrapped in an unprestrained EAP tape. The tape keeps the sphere aligned, yet allows relative movement between the spheres. Furthermore, the spheres are able to roll at the point of contact they make with each other. Also, the spheres provide the flexibility that the core requires for efficient movement, and are also able to support the axial loading due to the prestrained EAP layers. A number of test cores were built and tested, and repeatable results were observed. The deflection observed was between 5 to 7 degrees. The merit of this design was that the core is rigid and yet is able to bend. Though the core is not continuous (as it is made up of bead) it works as if it was, depending on the size of the beads. The spheres required, have to be light in weight and thus small beads were used. Since the diameter of the beads is small, therefore the moment is small, and we see small deflections. The prestrain of the DE EAP film keeps the spheres together. The main drawback is that since an unprestrained film of DE EAP is used to align the spherical beads, the film resists deflection upon actuation.

A second design based on a spherical core consisted of a core made of many lightweight

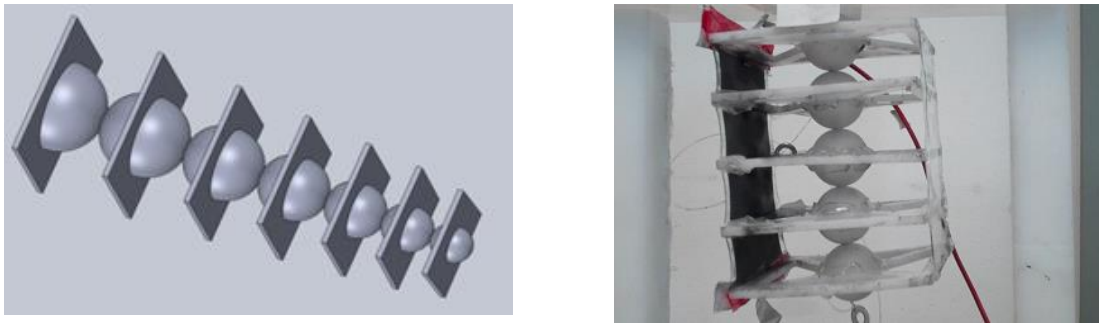

Figure 4.7: Spherical Core Design

spheres aligned in a line and connected by a string running through the length of the core. Square frames were attached to the equators of the spheres to provide attachment surfaces for the EAPs. The bending of the arm resulted from the spheres either sliding or rolling with respect to each other, and the rigidity of the spheres serve to maintain the prestrain of the EAPs. This design was very similar to the ball joint design, but was much easier to fabricate. The fabricated portion of this arm design had dimensions about 3 to 4 times bigger than the initial ball joint design. This allowed the EAPs to produce more force and a larger blocking moment. A 4 segment prototype of this design is showed in Figure 4.7. The spherical ball joint design of four segments actuated by one agonist-antagonist pair was subsequently fabricated to test its feasibility. The structural part includes the square frames and spherical balls connected axially through with a fishing line string. The the square frames were fabricated from HDPE using a CNC machine. Portions in the frames were machined out to minimize weight while still maintaining structural rigidity. In order to attach the DE EAP films onto the structure, the square frames of the four segments were first aligned relative to one another using screw attachments. This way the DE EAP films were attached to the structure without the structure moving in an undesired manner.

4.6 Tapered Design with Revolute Joint

Motivated by the previously-described design problems, we wanted a design that would reduce mass of the arm and provide flexibility. The taper can be linear, hyperbolic, parabolic or custom defined function. There are various design ideas for an arm with tapered core, one has a continuous core (Figure 4.6a) another has spherical balls as a core. The spherical ball core is made up of a composite core made up of spherical balls, foam, and HDPE frames which decrease in size along the length of the arm so that a tapered core is formed. The spherical balls can also be of decreasing diameter or the same diameter. The frames can be mounted on to the balls, and the balls will be aligned in a line and maintained in that alignment but a foam structure. The simplest design which has a taper is one with a revolute joint. It relatively easy to model, fabricate and has fewer components per module. In further discussion in the next chapter, we assume that the manipulator design is based on a series of tapered revolute actuator modules, that have been connected in series. Table 4.1 briefly summarizes different designs examined. All designs are compared with respect to weight of actuator module and type of manipulator designs.

Design	**Weight**	**Type**	**Comments**
Ball Joint	Bulky	Articulated	Due to weight considerations and large number of EAP films required to get high moment, this design not efficient/optimal.
EAP Core	Bulky	Continuous	The EAP muscle works because of its size but the EAP core wont work because it is bulky and cannot support the axial load adequately.
Flexible Core	Medium	Continuous	Moments are low thus it requires a large number of EAP films which will make it bulky.
Sphere Core	Light	Hybrid	Spheres roll over one another and resolution of movement depends on the size of the spheres
Tapered Core	Light	Hybrid	Taper angle can be varied and depending on that mass is reduced, the frames increase the moment

Table 4.1: Comparisons of various EAP arm designs

Chapter 5

DE EAP Actuator Module Mathematical Models

A model-guided approach is important for efficient design of actuator modules and a flexible manipulators. This Chapter, we use the material stress model defined in Chapter 3 for designing and analyzing actuator modules. Analysis for tapered actuator modules is presented in the subsequent sections. Using analytical model presented, we investigate how changing of design parameters affects the performance of the actuator modules. Note that such actuator modules can be used to fabricate full length flexible manipulators of given dimensions and performance requirements, that satisfy the design constraints.

5.1 Tapered Actuator Module

As we can see in Figure 5.1, the linear, parabolic and hyperbolic tapered designs have a varying lateral dimensions. Segments between the red circles represent actuator modules. The tapered manipulators will be fabricated using discrete actuator modules, it is important to carry out a parametric analysis to give insight into the design. Note, since the manipulators are discrete, thus each segment will have a fixed taper slope. We perform a study to investigate the electromechanical behavior of a tapered agonist-antagonist configuration with constant taper slope (Figure 5.2). Using this analysis, we want to achieve a design with optimal performance. These individual modules can then be arranged in series to fabricate complete manipulators. The support structure is assumed to have been made using HDPE. A single unit is first parametrically analyzed to determine the effects of changing parameters on free deflection angles. Using the parametric information, we can design manipulators sat-

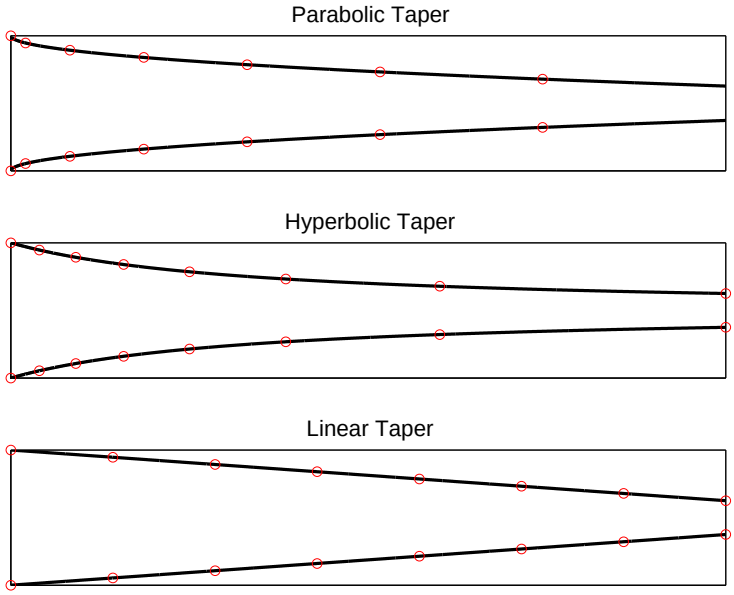

Figure 5.1: Flexible manipulator profiles: parabolic, hyperbolic and linear taper (from top to bottom). The red dots demarcate different actuator modules

isfying requirements for angle of deflection, blocking moment, length and number of modules specified. In this design, we can make each module to have optimal operating parameters but we cannot be sure that the full length manipulators designed are optimal.

5.2 Parametric Analysis

Illustrated in Figure 5.2, a single tapered actuator module in vertical orientation and neutral state. The coordinate frame used to describe the configuration is fixed on the revolute joint as indicated. The L length, B breadth and H and h heights are defined as indicated in Figure 5.2. Frame A with height H is grounded/fixed and cannot move. Frame B with height h is free to move upon actuation. In order to minimize the effect of bowing in of the prestrain DE EAP film, we assume $B \gg L$, which implies that prestrain in the y direction is approximately constant. Each DE EAP film stack has N layers of prestrained DE EAP films with predefined prestrains $\lambda_x \times \lambda_y$ and exerts a force F_i, where $i = l, r$. When neither DE film stack is activated the module is in neutral position. Upon activation, the new static

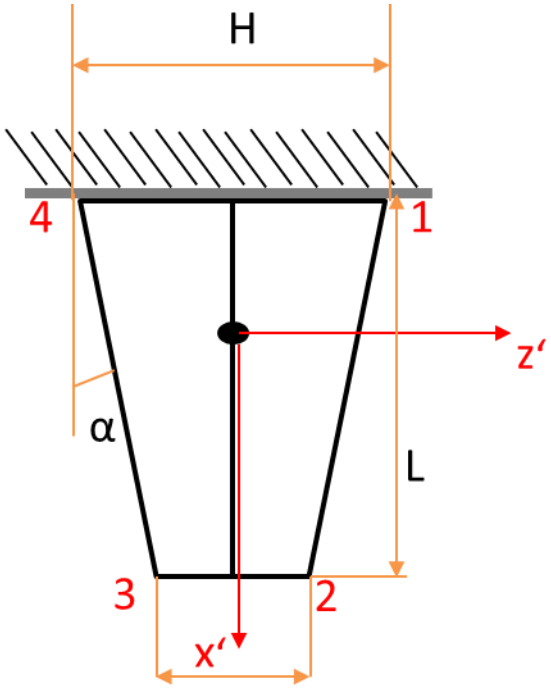

Figure 5.2: Linear taper actuator module schematic with dimensions

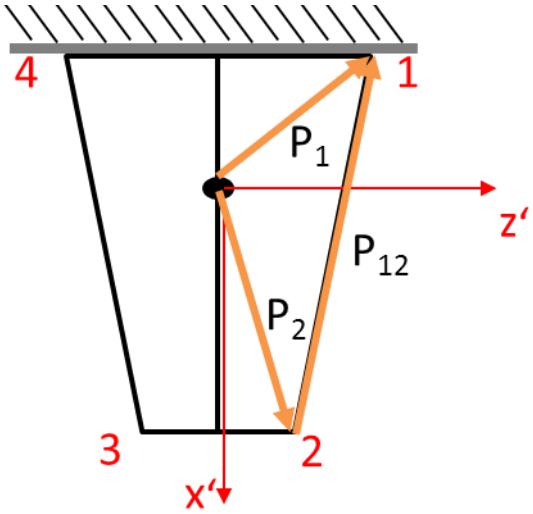

Figure 5.3: Linear taper actuator module with position vectors in neutral state

equilibrium depends on activation voltage and the geometry of the actuator. There will also be a force and corresponding moment due to weight of the support structure, core, and DE EAP films. As the total weight depends on materials used for fabrication, the initial analysis will ignore gravity. A second example analysis, with gravity included, will assume that the

fabrication material used is Hight Density Polyethylene (HDPE) and, the weight of the DE EAP film is negligibly small compared to the support structure.

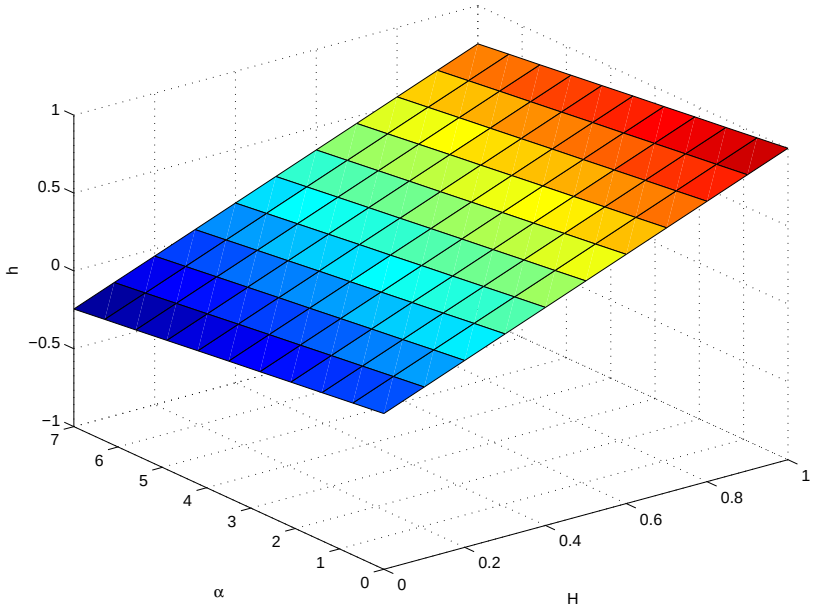

Figure 5.4: Taper angle α vs heights H and h

$$h = H - 2L\tan\alpha \tag{5.1}$$

The height dimensions H of frame A and h of frame B of the actuator module are related linearly by Eqn. (5.1). The taper angle is α and it is a constant for the linear actuator module case. For the analysis we normalize the dimensions, normalized heights are $h_n = \frac{h}{L}$ and $H_n = \frac{H}{L}$. The normalized distance of revolute joint is $d_n = \frac{d}{L}$. Figure 5.4 illustrates the relation between α and normalized H_n and h_n. We are interested in the region where $H_n > 0.5$. From previous work, we know that the number of layers doesn't affect the angle of deflection, but it does affect the blocking moment generated.

The force exerted by the DE EAP film is as in Eqn. (5.2). The $\frac{p}{K}$ term is the equivalent pressure term, as described in Chapter 3. As mentioned earlier to find the force per unit width we multiply the stress per unit width by the area of the DE EAP film in contact with

the frame.

$$F = NK\frac{L_z}{\lambda_x\lambda_y}(\lambda_x(\lambda_x - 1) - \frac{p}{K}) \tag{5.2}$$

$$\frac{p}{K} = \frac{1}{\lambda_x\lambda_y}(\frac{1}{\lambda_x\lambda_y} - 1) + \frac{\epsilon_o\epsilon_r}{\lambda_z^2}(\frac{U}{L_z^{(o)}})^2 \tag{5.3}$$

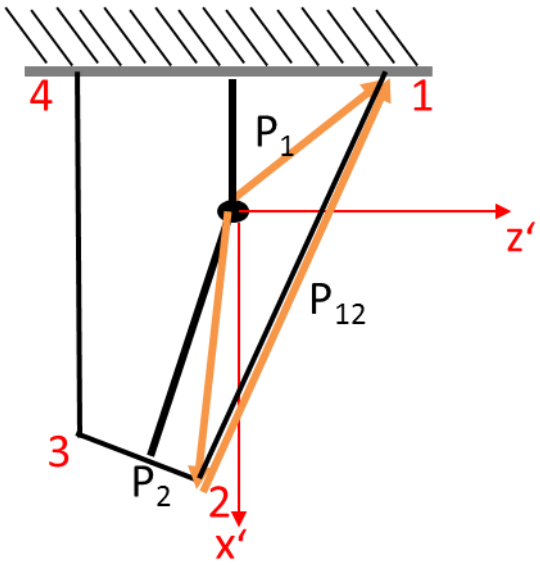

Figure 5.5: Linear taper actuator module with position vectors in activated state

For analysis, the position vectors $\mathbf{P}_i$ of point of action of of forces are required. Using the coordinate system $x' - z'$, as seen in Figure 5.5, we find the position vectors of points 1,2,3, and 4. It is assumed that the DE EAP film is attached to these points. Equations (5.4)-(5.7) define the position vectors in terms of h,H,L,d and deflection angle ϕ.

$$\mathbf{P}_1 = -d\,\hat{i} + H\,\hat{k} \tag{5.4}$$

$$\mathbf{P}_2 = [(L-d)\cos(\phi) + h\sin(\phi)]\,\hat{i} + [\frac{h}{2}\cos(\phi) - (L-d)\sin(\phi)]\,\hat{k} \tag{5.5}$$

$$\mathbf{P}_3 = [(L-d)\cos(\phi) - h\sin(\phi)]\,\hat{i} + [-\frac{h}{2}\cos(\phi) - (L-d)\sin(\phi)]\,\hat{k} \tag{5.6}$$

$$\mathbf{P}_4 = -d\,\hat{i} - H\,\hat{k} \tag{5.7}$$

These vectors are also used to determine the direction vectors $\mathbf{P}_{ij}$ of the forces. The

direction vector is obtained by summation of the relevant position vectors. Here, for example the direction vector from point i to point j is $\mathbf{P}_{ij} = \mathbf{P}_j + (-\mathbf{P}_i)$. To obtain the unit direction vector, we normalize it w.r.t its magnitude as shown in Eqn. (5.8) where $\mathbf{P}^n_{ij}$ is the normalized direction vector.

$$\mathbf{P}^n_{ij} = \frac{\mathbf{P}_{ij}}{||\mathbf{P}_{ij}||} \tag{5.8}$$

$$\mathbf{P}^n_{21} = \frac{\mathbf{P}_{21}}{||\mathbf{P}_{21}||} = \frac{\mathbf{P}_1 - \mathbf{P}_2}{||\mathbf{P}_1 - \mathbf{P}_2||} \tag{5.9}$$

$$\mathbf{P}^n_{34} = \frac{\mathbf{P}_{34}}{||\mathbf{P}_{34}||} = \frac{\mathbf{P}_4 - \mathbf{P}_3}{||\mathbf{P}_4 - \mathbf{P}_3||} \tag{5.10}$$

Furthermore, when the module is actuated, there will be changes in the lengths of the DE films. Thus the prestrain will change in order to attain a new static moment equilibrium. It is assumed that sufficient time has passed for the actuator to achieve static equilibrium. The new prestrains are determined using the position vectors and the initial prestrain λ^f_x as defined by Eqn. (5.11).

$$\lambda_x = \lambda^f_x \frac{||\mathbf{P}_{ij}||}{L_{\text{initial}}} \tag{5.11}$$

$$L_{\text{initial}} = \frac{L}{\cos(\alpha)} \tag{5.12}$$

Using the above unit vector, the vector expression for the force exerted by the DE film stack is the scalar product of the forces applied (F_r and F_l are for the right and left DE EAP films in Figure 5.3) and the direction vector as given in Eqns. (5.13) and (5.14).

$$\mathbf{F}_r = F_r \mathbf{P}^n_{21} \tag{5.13}$$

$$\mathbf{F}_l = F_l \mathbf{P}^n_{34} \tag{5.14}$$

Using the static moment equilibrium condition for the actuator module about the revolute

joint, we get a vector equatio, where $\mathbf{P}_i$ and $\mathbf{F_i}$ are from Eqns. (5.5), (5.6), (5.13), and (5.14). Using this equation we determine the deflection angle ϕ. Note Eqn. (5.15) is a function of ϕ only, as all other parameters are specified in ϕ. Thus solving Eqn. (5.15) gives us the value of ϕ for static equilibrium.

$$\mathbf{P}_2 \times \mathbf{F}_r + \mathbf{P}_3 \times \mathbf{F}_l = 0 \tag{5.15}$$

The static equilibrium when gravity is included is an in Eqn. (5.16). Where $\mathbf{r}$ vector is the position vector of the center of mass of the module and $\mathbf{g}$ is the acceleration due to gravity.

$$\mathbf{P}_2 \times \mathbf{F}_r + \mathbf{P}_3 \times \mathbf{F}_l + \mathbf{r} \times m\mathbf{g} = 0 \tag{5.16}$$

5.3 Results

Using the above modeling equations and setting the material parameters to fixed values ($K = 1.8e^{-4}, \quad e_o = 8.85e^{-12}, \quad e_r = 3.35,$ and $L_z = 1e^{-3}$), we analyzed the linear taper actuator model. The dimensions for the design were normalized w.r.t. the length L. For the analysis the prestrain are $\lambda_x \times \lambda_y = 3 \times 5$ and activation voltage is 3kV. The normalized parameters are varied to observe the effect on the performance. Note, solution for all configuration are not available as the module becomes unstable for some and no physically realizable solution can be found.

We can see from Figure 5.6, the relationship between the normalized distance of the revolute joint deflection angle for $H_n = 1$ and $\alpha = 1$ degree. The deflection angle ϕ first increases to a maximum value and then decreases. The curve is symmetric about the maximum deflection, for $d_n = 0.5$, and essentially has a bell shape. An important point to note is that the actuator module is unstable for $d_n = 0.5$, where we have maximum deflection, for small H_n. The DE film stack and the revolute joint may interfere, and the film might rip for this case. Also, as mentioned in [36] for the untapered module, as the stack approaches the revolute

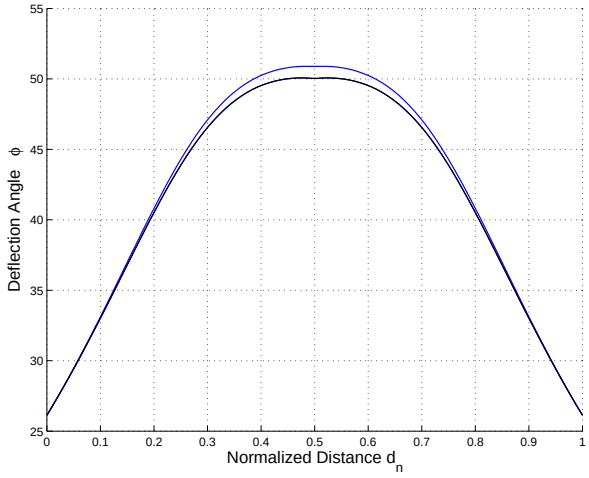

Figure 5.6: Deflection angle as d_n varies from zero to one. The blue curve neglects gravity. The black curve includes gravity.

joint, the lever arm will disappear, and no self-aligning torque is generated. Using information from the plot, we can optimize the design for different d_n, as per the requirements. As there is symmetry in the relation between angle of deflection and d_n, for simplicity we analyze the case for $d_n = 0$ or 1.

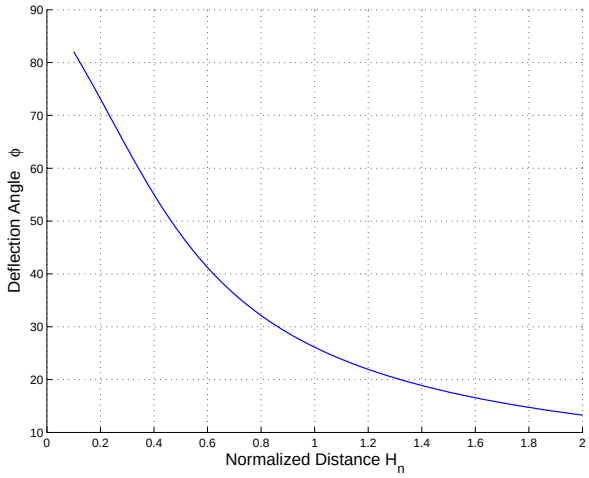

Figure 5.7: Deflection angle as H_n varies from 0 to 2, $d_n = 0$

As illustrated in Figure 5.7, the deflection angle decreases as H_n increases. As H_n becomes much bigger than 1, the deflection angle becomes very small.

Also, from the Figure 5.8 we find a linear relation between α and deflection angle. As α

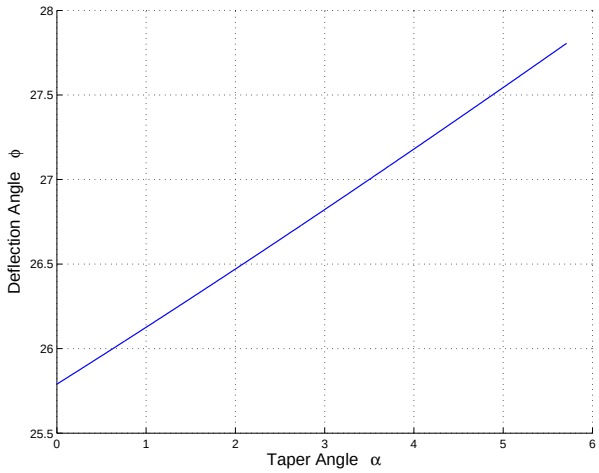

Figure 5.8: Taper angle α varied from 0-7 degrees, $d_n = 0$ and $H_n = 1$

is increased from 0 degrees, the deflection angle increases linearly. The increase in deflection angle as the taper angle changes is not much, hence we see that we can reduce the weight of the actuator module and subsequently, the whole manipulator without any decrease in the deflection angle. A comparison can be made between the untapered actuator module and tapered actuator modules. In Figure 5.9a, we can see difference in the deflection angle for the two cases. The tapered module has a taper angle $\alpha = 1$ degree. As we vary d_n, the deflection angle increases by a few degrees compared to the result reported in [36].

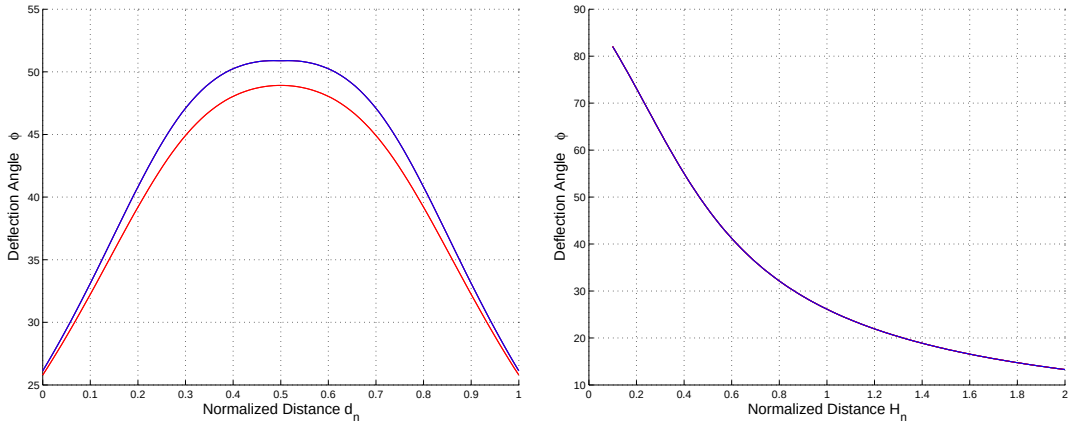

(a) Deflection angle as d_n varies (b) Deflection angle as H_n varies

Figure 5.9: Comparison between Taper Actuator Module and [36]

Therefore to design manipulators using modules, tapered actuator module can be used

instead of the untapered module. Since, deflection angles remain similar, but the weight of tapered module decreases, it is advantageous to use a tapered module.

Chapter 6

Mathematical Model of Central Pattern Generators

6.1 Introductory Remarks

Central pattern generators (CPGs) are neural networks that can produce rhythmic patterned outputs without rhythmic sensory or central input. These networks are present in both vertebrates and invertebrates animals. While designing a CPG network for bio-inspired robotic applications a few guidelines are required. The type and number of oscillators; the type and topology of couplings describe the general architecture of the network [27]. The synchronization conditions for the network of oscillators, i.e. the stable phase relations between oscillators depend on the architecture. The trajectories of the joint angles during each cycle is affected by the waveforms which are dependent on the shape of the limit cycle of oscillator [27], but can be transformed.

In this chapter, the Hopf Oscillator is presented which has been used for designing CPGs for control of bio-inspired robots [17, 44, 55]. Using contraction theory results, phase synchronization for a single chain Hopf oscillator network is proved. The technique used here for proving stable synchronization is based on results presented in [10, 11, 12, 42, 45]. Further, a few techniques such as fourier series, frequency splitting, and conformal mapping are discussed for pattern generation using network of Hopf oscillators.

6.1.1 Hopf Oscillator

The Hopf oscillator is named after a supercritical Andronov-Hopf bifurcation model with bifurcation parameter σ. When subcritical bifurcation occurs the system globally converges to the origin.

$$\dot{\mathbf{x}} = \mathbf{f}(\mathbf{x}; \omega; \rho; \sigma; \lambda) \tag{6.1}$$

$$\begin{bmatrix} \dot{u} \\ \dot{v} \end{bmatrix} = \begin{pmatrix} -\lambda(\frac{((u-a)^2+v^2)}{\rho^2} - \sigma) & -\omega \\ \omega & -\lambda(\frac{((u-a)^2+v^2)}{\rho^2} - \sigma) \end{pmatrix} \begin{bmatrix} u-a \\ v \end{bmatrix} \tag{6.2}$$

where $\mathbf{x} = (u; v)^T$ and $\omega, \sigma, \rho, \lambda$ are system parameters which can be adjusted. The Hopf oscillator has a limit cycle of radius ρ to which any trajectory exponentially converges with convergence rate $\lambda \geq 0$. The limit cycle oscillates with $\omega(t)$ which can be a time varying parameters. Note hopf oscillators can be considered to be phase-reduced oscillator which has been augmented to $\Re^2$ space [46].

6.1.2 Polar Transformation of Hopf Oscillator

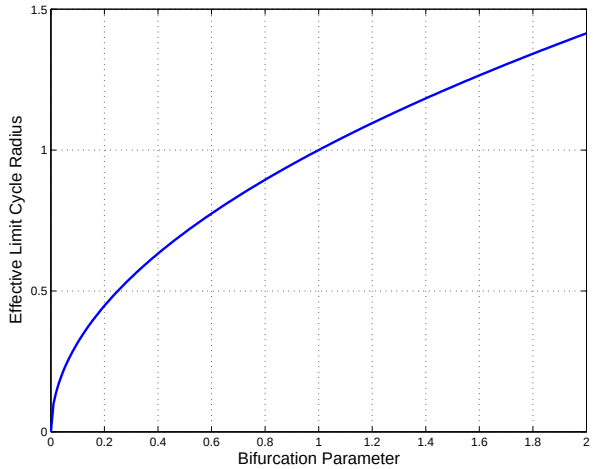

Figure 6.1: The radius of Hopf oscillator limit cycle vs the bifurcation parameter

Upon transforming into polar coordinates (substituting $x = r\cos\theta + a$ and $y = r\sin\theta$) we

get Eqn. (6.3).

$$\begin{bmatrix} \dot{r} \\ \dot{\theta} \end{bmatrix} = \begin{pmatrix} -\lambda r(\frac{r^2}{\rho^2} - \sigma) \\ \omega \end{pmatrix} \tag{6.3}$$

The Hopf oscillator equations have been decoupled and $\dot{r} = 0$ implies $r_{\text{eq}} = \sqrt{\sigma}\rho$. The effective limit cycle radius is dependent on bifurcation parameter and ρ as illustrated in Figure 6.1.

6.1.3 CPG Network Properties required for Phase Synchronization

We use Hopf oscillators because they are circularly symmetric, i.e. $\mathbf{f}(\mathbf{R}(\phi)\mathbf{x}) = \mathbf{R}(\phi)\mathbf{f}(\mathbf{x})$ for a 2-D rotation $\mathbf{R}(\phi)$. The scalability property of hopf oscillators, i.e. $\mathbf{f}(\gamma\mathbf{x}; \rho) = \gamma\mathbf{f}(\mathbf{x}; \frac{\rho}{\gamma})$ is also important. These properties are useful for establishing stable phase synchronization. For proving stable phase synchronization the coupled oscillator network graph should be balanced which implies that the number of edges in-degree of each node is equal to the out-degree [40].

6.2 Stable Synchronization of Hopf Oscillators

We can either have frequency synchronization in which, all the oscillators converge to a common frequency or phase synchronization in which, the oscillators oscillate with a desired phase difference. Here, by phase synchronization we mean an exact match of the scaled amplitude with a desired phase difference [10]. This will allow different actuators to oscillate at the same frequency but prescribed phase differences. In the CPG network, diffusive couplings are used to connect the oscillators. We prove stable phase synchronization of a single chain of coupled hopf oscillator using contraction theory. We consider a single chain network with n oscillators as shown in Figure 6.2.

Figure 6.2: Single Chain oscillator network with n Hopf oscillators

$$\begin{pmatrix} \dot{x_1} \\ \dot{x_2} \\ \vdots \\ \dot{x_n} \end{pmatrix} = \begin{pmatrix} f(x_1;\rho_1) - k(x_1 - \frac{\rho_1}{\rho_2}R(\Delta_{12})x_2) \\ f(x_2;\rho_2) - k\sum(x_2 - \frac{\rho_2}{\rho_i}R(\Delta_{2i})x_i) \\ \vdots \\ f(x_n;\rho_n) - k(x_n - \frac{\rho_n}{\rho_{n-1}}R(\Delta_{n(n-1)})x_{n-1}) \end{pmatrix} \tag{6.4}$$

Theorem 1. *In $\Re^n$, for a system $\dot{\mathbf{x}} = \mathbf{f}(\mathbf{x},\mathbf{t})$ where $\mathbf{f}(\mathbf{x},\mathbf{t})$ is a smooth nonlinear function, if there exists a square matrix $\mathbf{\Phi}(\mathbf{x},\mathbf{t})$ such that $\mathbf{M}(\mathbf{x},\mathbf{t}) = \mathbf{\Phi}(\mathbf{x},\mathbf{t})^T\mathbf{\Phi}(\mathbf{x},\mathbf{t})$ is a **positive definite metric** with $\mathbf{\Phi}(\mathbf{x},\mathbf{t})$ being a smooth differential coordinate transformation of the virtual displacement $\delta\mathbf{z} = \mathbf{\Phi}(\mathbf{x},\mathbf{t})\delta\mathbf{x}$ and the generalized Jacobian $\mathbf{F} = (\dot{\mathbf{\Phi}}(\mathbf{x},\mathbf{t}) + \mathbf{\Phi}(\mathbf{x},\mathbf{t})\frac{\partial \mathbf{f}}{\partial \mathbf{x}})\mathbf{\Phi}(\mathbf{x},\mathbf{t})^{-1}$ is **uniformly negative definite**, then irrespective of the initial conditions all trajectories of the nonlinear system globally converge exponentially to a single trajectory. The exponential rate of convergence is the largest eigenvalue of symmetric part $\mathbf{F_s}$ of $\mathbf{F}$. The nonlinear time-varying system is said to be **contracting** with $\mathbf{\Phi}(\mathbf{x},\mathbf{t})^T\mathbf{\Phi}(\mathbf{x},\mathbf{t})$ being the **contraction metric** for the system [10, 42].*

Theorem 2. *If the following condition is met uniformly for all $t > 0$, the any initial condition $\{x_o\}$ of the coupled Hopf oscillators in Eqn. (6.4) on a balanced graph converges to the flow invariant synchronized state Γ exponentially fast:*

$$V^T(\frac{\partial F}{\partial y} + \frac{\partial F^T}{\partial y})V < k(V^T\frac{L + L^T}{2}V) \tag{6.5}$$

where L is the laplacian matrix found using transformation matrix T and coupling matrix G. V is a matrix constructed using orthonormal eigenvectors of $\frac{L+L^T}{2}$ [10].

Theorem 1 is used for proving theorem 2. System of Eqns. (6.4) expressed in compact form as Eqn. (6.6):

$$\{\dot{x}\} = F(\{x\};\rho) - kG\{x\} \tag{6.6}$$

where k is the coupling gain, $F(\{x\};\rho) = [f(\{x_1\};\rho_1), f(\{x_2\};\rho_2), \ldots, f(\{x_n\};\rho_n)]$. The coupling terms are collected to construct the coupling matrix G for oscillator network in 6.2 as shown in Eqn. (6.7).

$$G = \begin{pmatrix} I_2 & \frac{-\rho_1}{\rho_2}R(\Delta_{12}) & 0 & \ldots & 0 \\ \frac{-\rho_2}{\rho_1}R(\Delta_{21}) & 2I_2 & \frac{-\rho_2}{\rho_3}R(\Delta_{23}) & \ldots & 0 \\ \vdots & \ddots & \ddots & \ddots & \vdots \\ 0 & \ldots & 0 & I_2 & \frac{-\rho_n}{\rho_{n-1}}R(\Delta_{n(n-1)}) \end{pmatrix} \tag{6.7}$$

For the network of oscillators shown in Figure 6.2, phase synchronization is achieved by $G\{x\} = 0$. Thus, from the phase synchronization condition we find the invariant subspace/manifold, from which we get Eqns. (6.8), (6.9) and so on for the other $n-2$ oscillators:

$$x_1 = \frac{\rho_1}{\rho_2}R(\Delta_{12})x_2 \tag{6.8}$$

$$x_1 = \frac{\rho_1}{\rho_3}R(\Delta_{13})x_3 \tag{6.9}$$

Therefore, the flow invariant space $\Gamma(\{x\})$ is:

$$\Gamma = x_1 = \frac{\rho_1}{\rho_2}R(\Delta_{12})x_2 = \frac{\rho_1}{\rho_3}R(\Delta_{13})x_3 \ldots = \frac{\rho_1}{\rho_n}R(\Delta_{1n})x_n \tag{6.10}$$

Note, once the system is in flow invariant space then it always remains there. Rewriting the flow-invariant subspace w.r.t to $x_1 = z_1$ so that the system becomes invariant to the phase differences and to different radii.

$$\Gamma(\{x\}) = z_1 = z_2 = \ldots = z_n \tag{6.11}$$

$$\Gamma\{x\} \iff \{z\} = T(\Delta_{ij}, \rho_i)\{x\} \tag{6.12}$$

The transformation matrix T is used to construct a conventional graph Laplacian matrix L using the relation of Eqn. (6.14). The Laplacian matrix constructed is for a balanced graph.:

$$T = \begin{pmatrix} I_2 & 0 & \dots & \dots & 0 \\ 0 & \frac{\rho_1}{\rho_2} R(\Delta_{12}) & \dots & \dots & 0 \\ \vdots & \ddots & \ddots & \ddots & \vdots \\ 0 & 0 & \dots & \dots & \frac{\rho_1}{\rho_n} R(\Delta_{1n}) \end{pmatrix} \tag{6.13}$$

$$L = TGT^{-1} \tag{6.14}$$

$$L = \begin{pmatrix} I_2 & -I_2 & 0 & \dots & \dots \\ -I_2 & 2I_2 & -I_2 & \dots & \vdots \\ \vdots & \dots & \dots & \dots & \vdots \\ 0 & \dots & \dots & -I_2 & I_2 \end{pmatrix} \tag{6.15}$$

Using the rotational and scaling properties of hopf oscillators explained in the previous section, we get Eqn. (6.16). From Eqn. (6.16) and (6.14) we get Eqn. (6.17).

$$TF(\{x\}; \rho) = TF(T^{-1}\{z\}; \rho) = F(\{z\}; \rho_1) \tag{6.16}$$

$$\dot{z} = F(\{z\}; \rho_1) - kL\{z\} \tag{6.17}$$

Now we constructed an orthonormal matrix V from orthonormal eigenvectors of $\frac{L+L^T}{2}$ which is the symmetric part of L. Note L is constructed using the flow invariant space Γ hence V is indirectly constructed from Γ. Using the results from [42] we know $VV^T + UU^T = I_{2n}$ where U is $\mathbf{1}$.

$$\{z\} = VV^T\{z\} + UU^T\{z\} \tag{6.18}$$

Premultiplying Eqn. (6.17) by V^T and substituting Eqn. (6.18) we get:

$$V^T\dot{z} = V^T F(VV^T\{z\} + UU^T\{z\}; \rho_1) - kV^T LVV^T\{z\} \tag{6.19}$$

We obtain an auxilary system (Eqn. 6.20) from Eqn. (6.19). Now we use contraction theory result of the auxilary system to find the condition stated in theorem 2.

$$\dot{y} = V^T F(Vy + 11^T\{z\}; \rho_1) - kV^T LVy \tag{6.20}$$

$y = V^T\{z\}$ is a particular solution and since $F(11^T\{z\}) \in \Gamma = Null(V)$ hence $y = 0$ is also a solution. Now if the system is contracting w.r.t y then the two solutions tend to each other. A system is contracting if the jacobian is uniformly negative definite as stated in [42]. Which implies if Eqn. (6.20) is valid then we have synchronization as long as the condition is valid.

$$V^T\frac{\partial F}{\partial y}(V^T y + 11^T\{z\})V - kV^T LV < 0 \tag{6.21}$$

$$V^T(\frac{\partial F}{\partial y} + \frac{\partial F^T}{\partial y})V - kV^T\frac{L + L^T}{2}V < 0 \tag{6.22}$$

$$V^T(\frac{\partial F}{\partial y} + \frac{\partial F^T}{\partial y})V < k(V^T\frac{L + L^T}{2}V) \tag{6.23}$$

$$\lambda_{\max}(V^T(\frac{\partial F}{\partial y} + \frac{\partial F^T}{\partial y})V) < \lambda_{\min}kV^T\frac{L + L^T}{2}V) \tag{6.24}$$

Using theorem 1, Eqn. (6.20) reduces to the condition of Eqn. (6.23) as in theorem 2. Now since the maximum eigenvalue of the jacobian in Eqn. (6.24) is less than equal to the convergence rate λ, thus the condition for stable synchronization boils down to $\lambda < \lambda_{\min(}kV^T\frac{L+L^T}{2}V)$.

6.3 Pattern Generation using CPGs

Some locomotion or movement of animals can be modeled by trajectories which have essentially sinusoidal time signals. But most real locomotion trajectories of mammals, amphibians or aquatic creatures are complicated than sinusoidal time signals that a network of coupled Hopf oscillators may generate. Thus, it becomes important to find ways to morph/modulate signals so that appropriate trajectories can be generated or approximated. If the trajectories are known apriori from experiments or dynamic modeling, then it may be possible to generate patterns of locomotion/movement with some approximation. In this section, few methods based on Fourier series, conformal mapping and frequency splitting for pattern generation are discussed.

6.3.1 Pattern Generation Using Fourier Series

Periodic signals or functions can be decomposed into a sum of oscillating sinusoidal functions using Fourier series. A pattern can be generated by constructing a truncated Fourier series approximation that has frequencies in multiples of the base frequency ω. In Figure 6.3, two examples for pattern generation are illustrated. The signal outputs are summed with appropriate weights according to Fourier decomposition and we get a periodic signal approximating the first two terms of a Fourier series.

For two layered CPGs shown in Figure 6.4a, we have two single chain CPGs. The frequency of one is ω and the other is 2ω (Figure 6.4a). The outputs of two adjacent oscillators are combined with appropriate weights, w_i (Eqn. (6.25)), to generate the periodic signals A, B, and C, as seen in Figure 6.4b. Signals A, B, and C are the blue, red and black signals in 6.4b. In Eqn. (6.25), the weights used signal A are 2 and -1 and for signals B and C all weights are 1. The phase difference between oscillators is prescribed as $\frac{\pi}{6}$.

$$y_i = w_{i1}x_{i1} + w_{i2}x_{i2}, \quad \text{i=A,B and C} \tag{6.25}$$

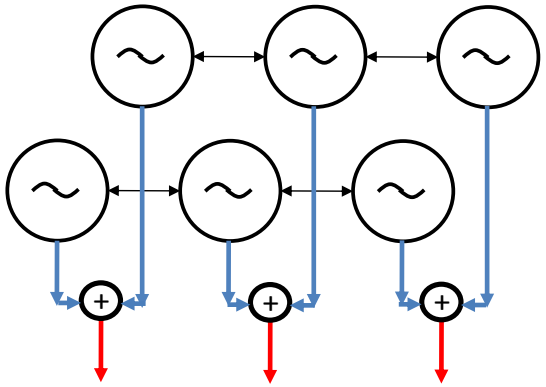

(a) Two Layered CPG Pattern Generation

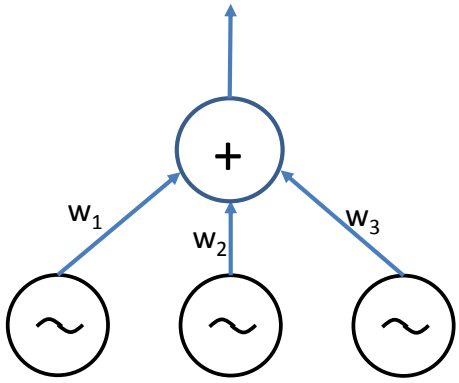

(b) Three oscillators used to construct an approximate saw-tooth waveform

Figure 6.3: Pattern Generation using Fourier Sums

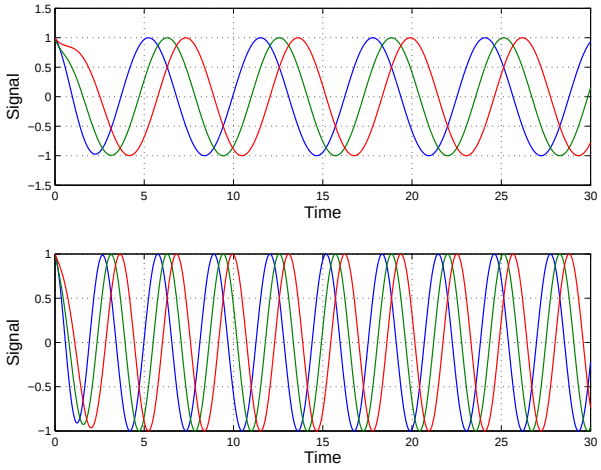

(a) Signals with frequency ω and 2ω

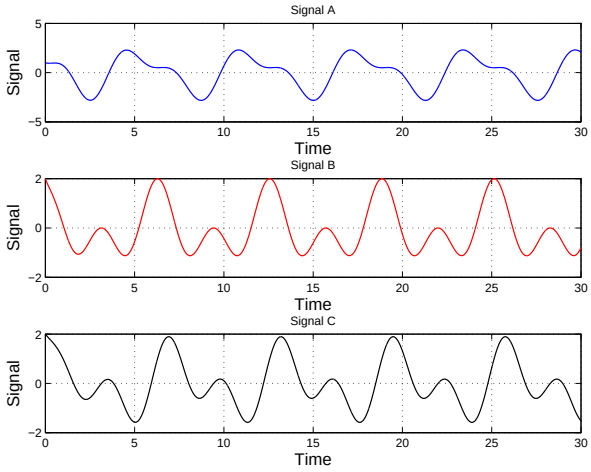

(b) Generated signals A, B and C

Figure 6.4: MATLAB simulation for two layered CPG

For a more illustrative example, we decompose a saw tooth signal (6.26a) into three Fourier terms and sum them with appropriate weights to generate an approximate signal. To find the weights, we find the first three terms for approximating the sawtooth waveform. The coefficients for the three term Fourier series are found using Eqns. (6.26b) - (6.26d). Eqn. (6.26e) is the approximated sawtooth waveform equation. Using the terms from Eqn. (6.26e), appropriate oscillator frequencies and weights are found and used to generate the sawtooth

waveform using Hopf oscillators. Figure 6.5 shows the MATLAB generated waveforms.

$$F(x) = \frac{x}{\pi}; \quad -\pi < x < \pi \tag{6.26a}$$

$$a_0 = \frac{1}{\pi}\int_{-\pi}^{\pi} \frac{\mathrm{x}}{\pi}\,\mathrm{d}x = 0 \tag{6.26b}$$

$$a_n = \frac{1}{\pi}\int_{-\pi}^{\pi} \frac{\mathrm{x}}{\pi}\cos(\mathrm{nx})\,\mathrm{d}x = 0 \tag{6.26c}$$

$$b_n = \frac{1}{\pi}\int_{-\pi}^{\pi} \frac{\mathrm{x}}{\pi}\sin(\mathrm{nx})\,\mathrm{d}x = 2\frac{-1^{n+1}}{n} \tag{6.26d}$$

$$f(x) = 2\sin(x) - \sin(2x) + \frac{2}{3}\sin(3x); \quad -\pi < x < \pi \tag{6.26e}$$

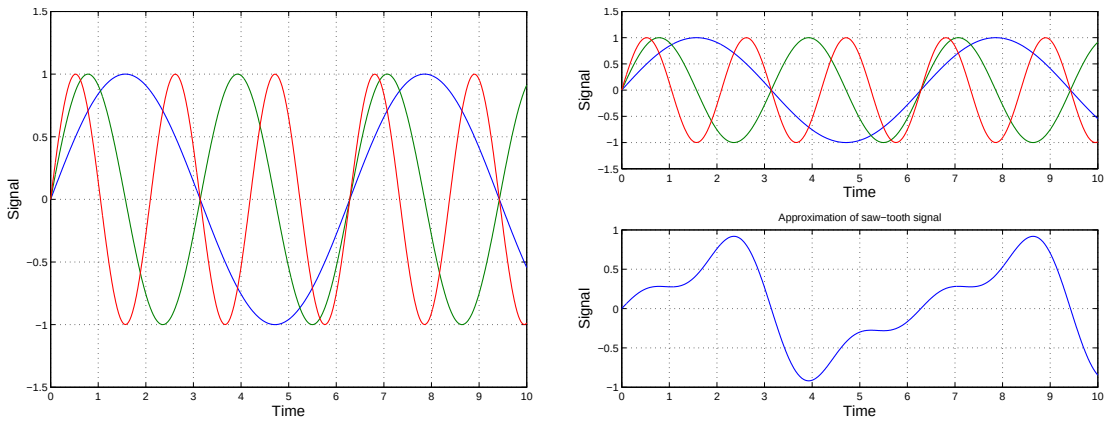

(a) Periodic sawtooth waveform (b) Approximate saw-tooth waveform

Figure 6.5: Pattern generation of sawtooth waveform

6.3.2 Frequency Splitting

The frequency of oscillation can be changed during each cycle. The frequency split can be controlled for appropriate pattern generation. In Figure 6.6, a signal from a single oscillator, having two frequencies of oscillation is illustrated. The change occurs based on a predefined condition which can be tuned to according to the requirements. For the example, toggling

is used for frequency split. As v, a state variable of the Hopf oscillator, changes sign the frequency changes.

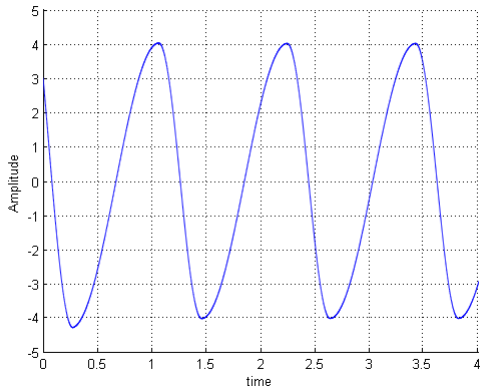

Figure 6.6: Wave form generated by frequency splitting

6.3.3 Conformal Mapping for Transformation

We investigate conformal mapping to transform the Hopf oscillator to get desired waveforms and limit cycles. We study simple functions like translation, scaling, rotation, and inversion. These functions can be used to construct more complicated conformal mapping functions. We are interested in conformal mapping as conformal functions preserve angles which we want for the trajectories in state space. It is interesting to note that the aforementioned transformations maintain the circular symmetry property. A way to use conformal mapping for Hopf oscillator is to combine individual transformations or form commutative functions to generate required patterns. Also, if a trajectory waveform is know apriori, then using an appropriate conformal mapping, we can construct the waveform using the Hopf oscillator. Basic mappings are briefly studied, and we use the following convention. Signal outputs x and y of the oscillator are real and complex parts respectively in z, b is a constant and u and v are the mapped signals in $g(z)$.

$$z = e^{\iota\theta} = x + iy, \quad b = b_x + b_y, \quad g(z) = u + iv$$

Translation

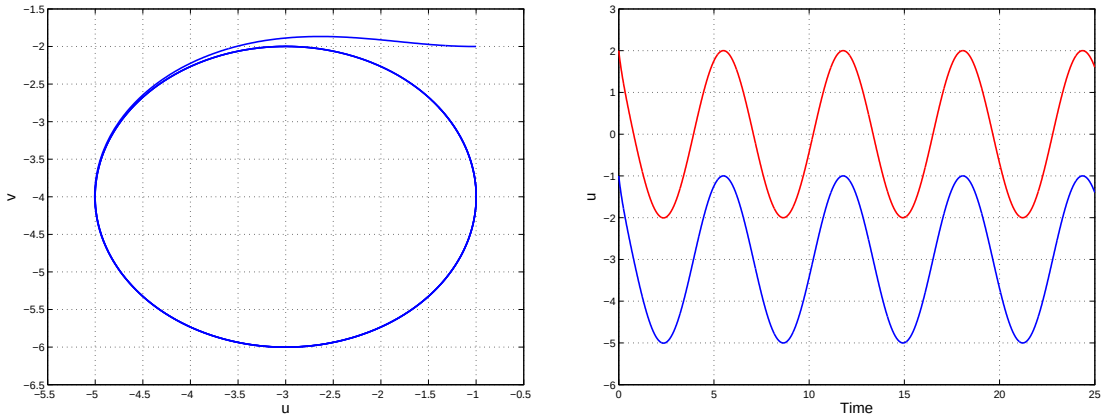

(a) Limit cycle of oscillator after conformal translation

(b) Waveform for translation: Red - original waveform. Blue - mapped waveform

Figure 6.7: Conformal mapping: translation

$$g(z) = (x + b_x) + i(y + b_y), \quad x = u - b_x, \quad y = v - b_y \tag{6.27a}$$

$$\begin{bmatrix} \dot{u - b_x} \\ \dot{v - b_y} \end{bmatrix} = \begin{bmatrix} -\lambda(\frac{((u-b_x)^2+(v-b_y)^2)}{\rho^2} - \sigma) & -\omega \\ \omega & -\lambda(\frac{((u-b_x)^2+(v-b_y)^2)}{\rho^2} - \sigma) \end{bmatrix} \begin{bmatrix} u - b_x \\ v - b_y \end{bmatrix} \tag{6.27b}$$

Eqn. (6.27a) defines the translation conformal mapping for state variables. Using (6.27a) we derive Eqn. (6.27b) for the oscillator after mapping has been done. The unstable equilibrium point at 0 shifts by b. The phase and amplitude remain unchanged. The waveform shifts by a bias (Figure 6.7b) and the limit cycle is centered around b (Figure 6.7a).

Scaling

$$g(z) = cx + icy, \quad x = u/c, \quad y = v/c \tag{6.28a}$$

$$\begin{bmatrix} \dot{u} \\ \dot{v} \end{bmatrix} = \begin{bmatrix} -c\lambda(\frac{(u/c^2+v/c^2)}{\rho^2} - \sigma) & -c\omega \\ c\omega & -c\lambda(\frac{(u/c^2+v/c^2)}{\rho^2} - \sigma) \end{bmatrix} \begin{bmatrix} u/c \\ v/c \end{bmatrix} \tag{6.28b}$$

Eqn. (7.1) defines the scaling conformal mapping for state variables. Using Eqn. (7.1) we derive Eqn. (7.2) for the oscillator after mapping has been done. The equilibrium points

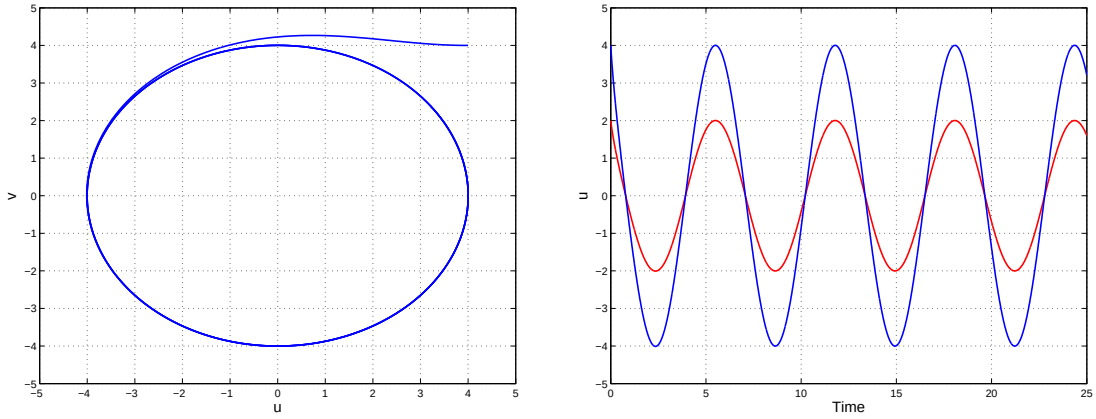

(a) Limit cycle of oscillator after conformal scaling

(b) Waveform for scaling : Red - original waveform. Blue - mapped waveform

Figure 6.8: Conformal mapping: scaling

remain at the same position and the phase does not change. The amplitude increases by the scaling factor$c$ (Figure 6.8b). The limit cycle radius increases by the scaling factor (Figure 6.8a).

Rotation

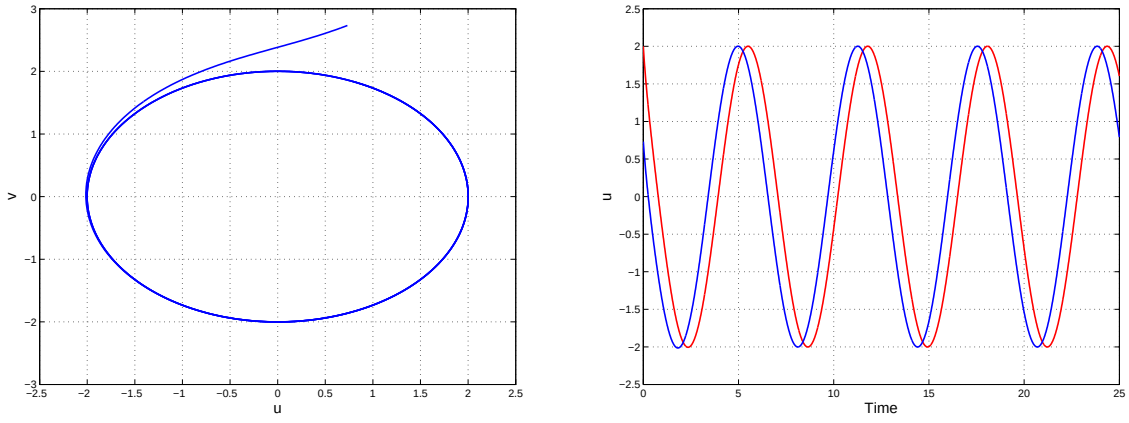

(a) Limit Cycle of oscillator after conformal rotation

(b) Waveform of rotation : Red - original waveform. Blue - mapped waveform

Figure 6.9: Conformal mapping: rotation

$$g(z) = [x\cos(\phi) - y\sin(\phi)] + i[-x\sin(\phi) + y\cos(\phi)] \tag{6.29a}$$

$$x = u\cos(\phi) + v\sin(\phi), \quad y = v\cos(\phi) - u\sin(\phi) \tag{6.29b}$$

$$\begin{bmatrix} \dot{u} \\ \dot{v} \end{bmatrix} = \begin{bmatrix} -\lambda(\frac{(u^2+v^2)}{\rho^2} - \sigma) & -\omega \\ \omega & -\lambda(\frac{(u^2+v^2)}{\rho^2} - \sigma) \end{bmatrix} \begin{bmatrix} u \\ v \end{bmatrix} \tag{6.29c}$$

Eqn. (6.29a) defines the rotation conformal mapping for state variables. Using Eqn. (6.29a) we derive Eqn. (6.29c) for the oscillator after mapping has been done. The equilibrium points remain unchanged. The amplitude remains the same but the phase changes by the angle of rotation (Figure 6.9).

Inversion

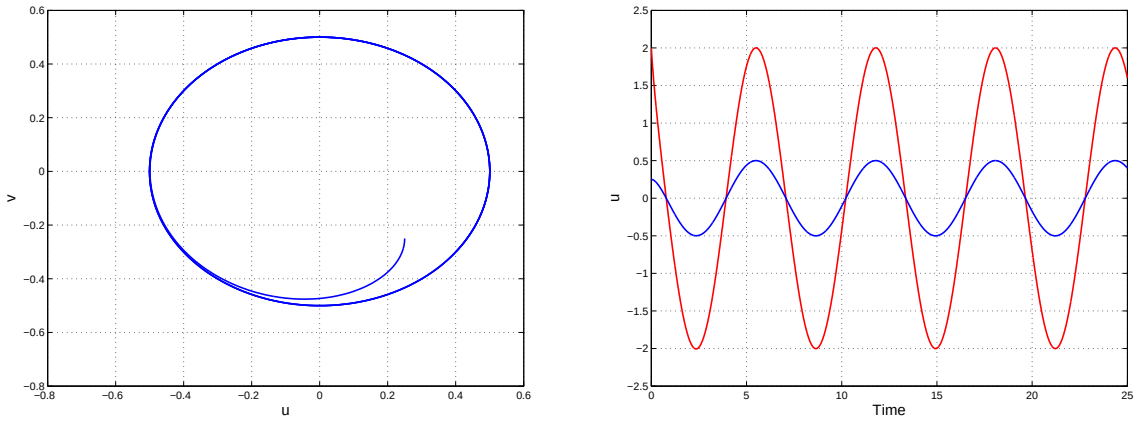

(a) Limit cycle of oscillator after conformal inversion

(b) Waveform of inversion : Red - original waveform. Blue - mapped waveform

Figure 6.10: Conformal mapping: inversion

$$g(z) = \frac{x}{x^2+y^2} - i\frac{y}{x^2+y^2}, \quad x = \frac{u}{u^2+v^2}, \quad y = -\frac{v}{u^2+v^2} \tag{6.30a}$$

$$\begin{bmatrix} \dot{u} \\ \dot{v} \end{bmatrix} = \begin{bmatrix} \lambda(\frac{1}{\rho^2(u^2+v^2)} - \sigma) & \omega \\ -\omega & \lambda(\frac{1}{\rho^2(u^2+v^2)} - \sigma) \end{bmatrix} \begin{bmatrix} u \\ v \end{bmatrix} \tag{6.30b}$$

Eqn. (6.30a) defines the inversion conformal mapping for state variables. Using Eqn. (6.30a) we derive Eqn. (6.30b) for the oscillator after mapping has been done. Illustrated in Figure

6.10, the amplitude reduces by a factor of ρ^2. The limit cycle become clockwise instead of counter-clockwise.

Conformal mapping can be used for transformation of state space and waveforms, and the four basic mapping examined above may be combined to make new waveforms. The use of conformal mapping is limited due to difficulty in finding analytical expressions for required waveforms. Also, conformal mappings may or may not form composite mapping , and thus there are more limitations. For example, the composite mapping formed by first translation, and then rotation is different from that formed by rotation, and then translation.

Chapter 7

Octopus-based Control using CPGs

7.1 Motion Primitives

The intrinsic nature and design of an octopus arm, permits it to perform a large number of different motions ranging from manipulation of objects to swimming. Some of these motions can be broken down into simpler motion primitives which can be combined to achieve a certain task. A few of these, such as elongation/contraction, bend formation, bend propagation, and fetching have been identified [5, 18]. In [53] 3-D reconstruction was used for analyzing movements of an octopus arm and identify motion primitives. Vavourakis V. and et al. [49], presented primitive behaviour generations in a nonlinear hyperelestic robotic arm. In [49], octopus inspired arm was simulated using a finite element framework and suitable activation functions were defined to generate different primitives.

To control a flexible manipulator, we suggest using CPGs and varying the CPG parameters. Since $\omega(t)$ can be time varying, we can vary it to position the flexible arm in a particular configuration. Furthermore, by changing the bifurcation parameter at the right instant in time, we can also control the configuration of the arm. The velocity of the arm segments can be controlled either by $\omega(t)$ or by a time varying rate of convergence depending on how we intend to achieve the particular configuration. We briefly discuss below the basic motion primitives/stereotypes identified in [18] of an octopus arm.

7.1.1 Octopus Arm Bending Primitive

Bend formation is a most important and basic motion primitive. Bends can be formed anywhere along the length of the arm depending on the goal of motion [5, 18, 50]. The muscles in the region of the bend, contract and expand for bend formation. To form a bend in the manipulator, CPG parameters are set to appropriate values depending on the objective. We suggest to use the bifurcation feature of Hopf oscillator for bending.

7.1.2 Reaching Primitive of Octopus Arm

A bend propagation or wave propagation from the base of the arm towards the tip of the arm accomplishes reaching or extension of arm. The arm is initially in a bent position. A activation wave propagates along the length of the arm starting at the root of the arm [5, 18, 50].

7.1.3 Elongation/Contraction Primitive

Octopus arm muscles can contract or elongate along the length of the arm. Since, an octopus arm is a muscular hydrostat the volume is almost constant during elongation or contraction [5].

7.1.4 Grasping Primitive of Octopus Arm

Grasping primitive is used to get hold of an object. The arm wraps around the target object. Since, an octopus arm has suckers on it, the grip is quite strong. Once the arm makes contact with the object, the arm which extends beyond the point of contact starts to pivot about that point and assume a inner shape depending on the shape of the object to be grasped. The grasping can be whole arm grasping or partial arm depending on the objective of grasping.

7.1.5 Fetching Primitive of Octopus Arm

Octopus and primate arm morphology is quite different with the former being a hydrostatic structure without a skeletal support structure and the latter being three rigid joints actuated by muscles attached to a skeletal structure. Despite these difference, an analogy between the two can be estaiblished for achieving the fetching motion [48]. The octopus arm stiffens into a quasi-articulate three joint structure which functions similarly to a primate arm. This kind of reconfiguration of the arm provides a precise and efficient point-to-point movement between desired points. For this motion stereotype we use the standard kinematic model for three link manipulator [5].

7.1.6 Sculling Primitive for Swimming

Sculling motion primitive is used for swimming. It is not the primary propulsive mode but complements the jet stream used by octopus to swim. In a simple sculling mode, propulsion is achieved by two-stroke motions of the arms. Sculling has two modes: 1) Without undulations (Figure 7.1a) and 2) With undulations (Figure 7.1b). The kinematics of arm swimming has not been investigated in detail, although one essential feature, extracted from related data, is that each stroke comprises two phases. First the arms, initially trailing behind the octopus body, open by bending outwards relatively slowly (recovery stroke), and second, when they return fast to their initial position (power stroke) [47].

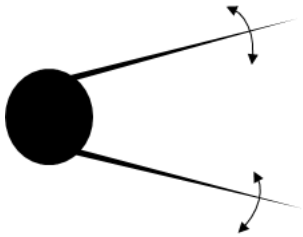

(a) Sculing without undulations

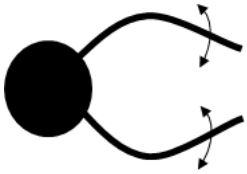

(b) Sculling with undulations

Figure 7.1: Sculling motion primitive

7.2 Octopus Arm Bending

We investigate a simple case of a single link. In bifurcation control two strategies are proposed. Each manipulator segment has a Hopf oscillator to provide control. The two strategies differ with respect to ω. In the first strategy we set $\omega = 0$ for the duration of motion. In the second strategy ω varies according to some function and we take it to zero when we want the manipulator segment motion to cease. The other oscillator parameters can be time varying depending on the requirements of the arm motion. We begin the discussion using these control strategies for a single segment.

7.2.1 Using Bifurcation for Bending

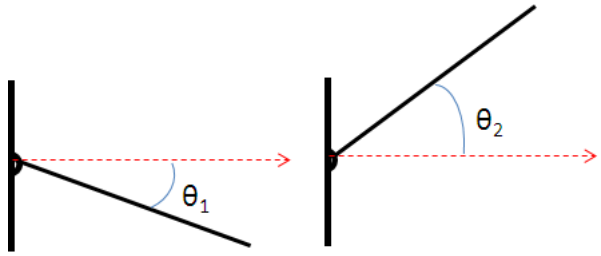

Figure 7.2: Single segment manipulator

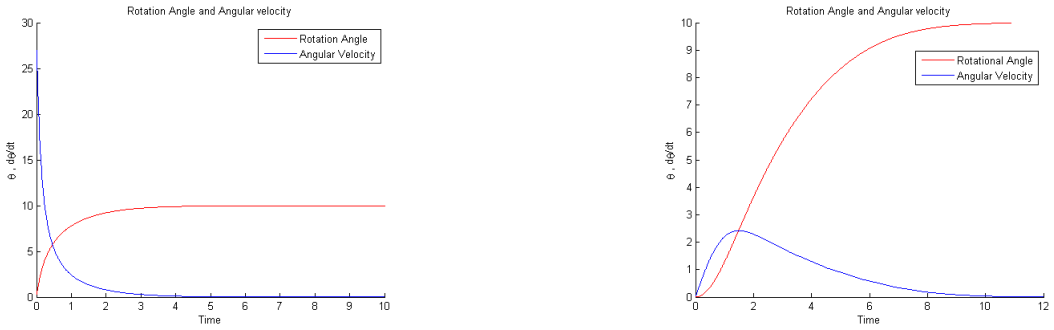

(a) Fixed parameters (b) Time varying parameters

Figure 7.3: Angular displacement and angular velocity for single segment

We investigate the case when we have a single segment and ω is small. If the initial position of link is θ_1 and the, final position is θ_2 then angular rotation required is $\theta_2 - \theta_1 = \theta_{12}$. Figure

7.3 illustrates the angular displacement and angular velocity profile for both time vary and invariant parameters values. The amplitude $\rho = 1$, bias $a = 1$, and bifurcation parameter $\sigma = -1$ are fixed for both cases. The convergence rate is $\lambda = 1$ for the time invariant case and for the time varying case, $\lambda = \frac{1}{t}$.

7.2.2 Bend Formation in Manipulator with N Links

A manipulator with N segments can be controlled by using N Hopf oscillators. Each segment has a Hopf oscillator controlling it with it's own set of paramters. Bend formation for a 10 link manipulator using bifurcation was simulated using simulink. Figure 7.4 illustrates an example for bend formation. The bias for each oscillator is set at 9 degrees. The frequency and amplitude of oscillation which are set as .01 rad/s and 30 degrees, do not significantly effect bend formation for convergence rate $\lambda > 1$.

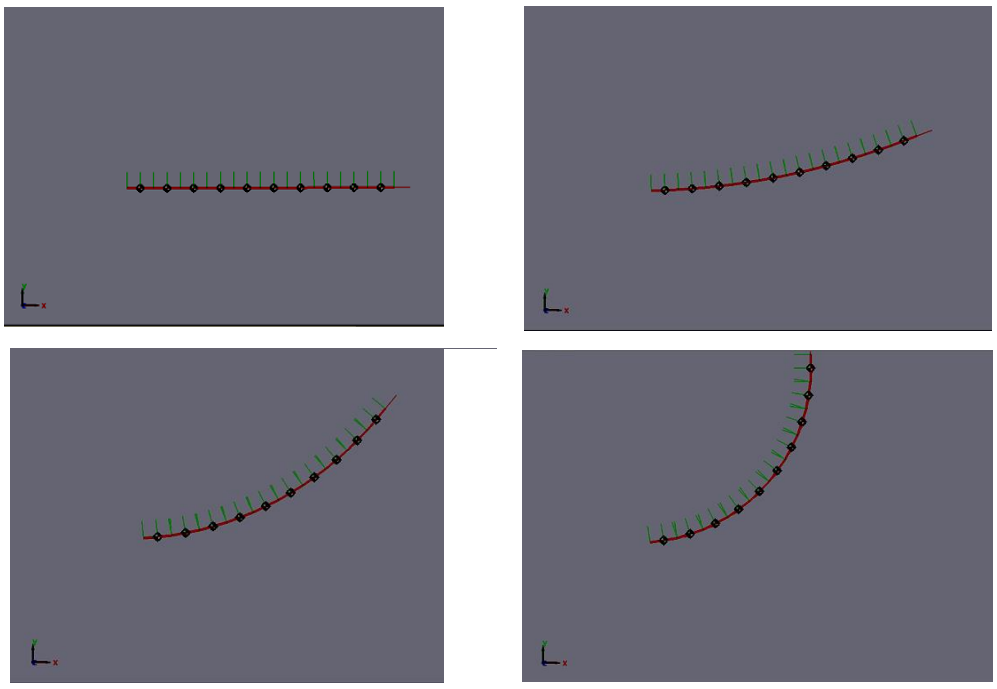

Figure 7.4: Simulink simulation of bend formation in manipulator using CPGs.

For the case in Figure 7.4 the bias parameter had same value and the convergence rate was constant. In the top row, from left to right we have initiation of bend and in the bottom row,

from left to right bend formation ends. By varying these parameters different configurations can be achieved as required.

7.3 Sculling With Undulation

We only examine sculling without undulations. The arm remains straight with rotation happening only at the base or the root of the arm. The root is controlled using a Hopf oscillator. Sculling mode has two strokes in a single cycle, one is the power stroke, and the other is the recovery stroke. The stroke velocities are different for power and recovery stroke. We use Eqns. (7.1) and (7.2) are for sculling mode derived in [47]. These equations represent the angle, the root of the octopus makes with the axial axis along it's body.

$$\phi(t) = (\phi + \alpha) - 2\alpha\frac{t(\beta+1)}{T_s}, \quad 0 < t < \frac{T_s}{\beta+1} \tag{7.1}$$

$$\phi(t) = (\phi - \alpha) + 2\alpha\frac{t(\beta+1) - T_s}{\beta T_s}; \frac{T_s}{\beta+1}, \quad < t < T_s \tag{7.2}$$

From Eqns. (7.1) and (7.2), we note that the period of oscillation is $T_s = 2\alpha\frac{\beta+1}{\beta\omega}$. The power

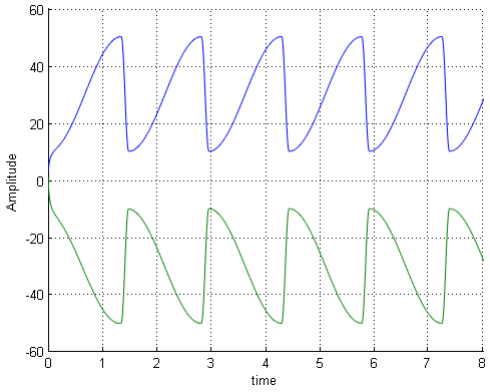

Figure 7.5: Sculling mode with two frequencies cycle

and recovery stroke have the same oscillation amplitude. Using the fact that each stroke has to cover π phase angle, we find the oscillation frequencies ω_1 and ω_2 for the two strokes. For

the power stroke the frequency relationship is defined in Eqn. (7.1). The recovery stroke frequency relation is defined in Eqn. (7.2). The parameters $\alpha = 20$ degrees which is the bias angle, $\beta = 6$ is the ratio of velocities of the recovery and power strokes and $\omega = 40$ degrees/s is the constant angular velocity of the arms.

$$2\pi = \int_0^{\frac{T_s}{\beta+1}} \omega_2 \, \mathrm{d}t + \int_{\frac{T_s}{\beta+1}}^{T_s} \omega_1 \, \mathrm{d}t, \quad \omega_1 = \frac{\pi\beta\omega}{2\alpha}, \quad \omega_2 = \frac{\pi\beta\omega}{2\alpha} \tag{7.3}$$

Using the frequency relation derived above we simulate the sculling mode in MATLAB. Two oscillators are coupled with π phase difference. Oscillations occur at two frequencies (60 Hz and 366 Hz) during a cycle, and the change is controlled using the output of one of the oscillators. Figure 7.5 illustrates the CPG output signals which can be used for simulating sculling mode without undulations. The two signals are out of phase by π, similar to the octopus swimming motion. Thus, CPGs constructed using Hopf oscillator can be used for generation of some motion primitives.

Chapter 8

Conclusion

The overall purpose of this thesis was to investigate the feasibility of using dielectric electroactive polymers for design of flexible actuators/manipulator technologies and also to examine central pattern generators for control of such flexible manipulator systems. For this purpose, a literature review was done to identify the current EAP technologies. Conceptual designs of various actuator modules and manipulators were proposed. Using material model developed in [36], a model-guided approach was used for designing and prototyping of modules. The prototypes fabricated in the lab, were tested for their performance. The tests shed light on the feasibility of use of DE EAP material and its reliability.

The actuator modules failed after being actuated a couple of times. Failure also occured with or without actuation after a few days, as relaxation occurs in the prestrained film and prestrain decreases. It was also evident that the reliability of the DE EAP actuators relied heavily on the fabrication process. Therefore, a process was developed to handle the prestrain DE EAP films and apply electrode material with due care. It was also found that the support structures for the actuator modules need to be flexible and at the same time, be able to support the axial loading due to prestrained DE EAP film.

It was found that for a simple DE EAP actuator module, design analysis using a material model is feasible. A model for a tapered actator module was developed. The design simulations using the model for a tapered actuator module design suggested that the performance of the tapered module was as good as that of the actuator module developed in [36] with the added advantage of lower weight of the overall system. The tapered actuator module could be used to fabricate a full-length flexible manipulators according to design requiements. Al-

though DE EAP has some potential to be used for development of flexible actuators, but further improvements are required in the material properties like higher Young's modulus, lower activation voltages in the order of 100s of volts instead of 1000s of volts.

In addition to DE EAP actuators, engineered CPG models were studied with the phase synchronization condition for a single chain Hopf oscillator. The single chain oscillator network can be used for control of various bio-robotic systems, like snake robots, inchworm robots, and worm robots. The proposed techniques for pattern generation using fourier series seem to be promising and the few examples studied showed how they can be used. Frequency splitting and conformal mapping were also studied and might have potential for generation of rhythmic patterns using CPGs. Also, the mapping of phase trajectory might not have analytical relations. Furthermore, motion primitives for octopus arm motion were identified from the literature. An attempt was made to implement bend formation and sculling using CPGs. These motion primitives are non-rhythmic in nature and thus using CPGs may not be feasible. For implementing CPGs based control in biomimetic robots, further work is required develop control laws based on animal motion primitives.

References

[1] http://actuatorweb.org/index.php?page=summary.

[2] http://ndeaa.jpl.nasa.gov/nasa-nde/lommas/eap/actuators-comp.pdf.

[3] http://www.empa.ch/plugin/template/empa/*/72289/—/l=1.

[4] J. S. Bay and H. Hemami. Modeling of a neural pattern generator with coupled nonlinear oscillators. *Biomedical Engineering, IEEE Transactions on*, (4):297–306, 1987.

[5] D. T. Branson, R. Kang, E. Guglielmono, and D. G. Caldwell. Control architecture for robots with continuum arms inspired by octopus vulgaris neurophysiology. In *Robotics and Automation (ICRA), 2012 IEEE International Conference on*, pages 5283–5288. IEEE, 2012.

[6] D. B. Camarillo, C. F. Milne, C. R. Carlson, M. R. Zinn, and J. K. Salisbury. Mechanics modeling of tendon-driven continuum manipulators. *Robotics, IEEE Transactions on*, 24(6):1262–1273, 2008.

[7] F. Carpi, A. Khanicheh, C. Mavroidis, and D. De Rossi. Silicone made contractile dielectric elastomer actuators inside 3-tesla mri environment. In *Intelligent Robots and Systems, 2008. IROS 2008. IEEE/RSJ International Conference on*, pages 137–142. IEEE, 2008.

[8] F. Carpi, A. Migliore, and D. De Rossi. A new contractile linear actuator made of dielectric elastomers. In *Smart Structures and Materials*, pages 64–74. International Society for Optics and Photonics, 2005.

[9] K.-J. Cho and H. H. Asada. Architecture design of a multiaxis cellular actuator array using segmented binary control of shape memory alloy. *Robotics, IEEE Transactions on*, 22(4):831–843, 2006.

[10] S.-J. Chung and M. Dorothy. Neurobiologically inspired control of engineered flapping flight. *Journal of guidance, control, and dynamics*, 33(2):440–453, 2010.

[11] S-J. Chung and J.-J. Slotine. On synchronization of coupled hopf-kuramoto oscillators with phase delays. In *Decision and Control (CDC), 2010 49th IEEE Conference on*, pages 3181–3187. IEEE, 2010.

[12] S.-J. Chung and J.-JE. Slotine. Cooperative robot control and concurrent synchronization of lagrangian systems. *Robotics, IEEE Transactions on*, 25(3):686–700, 2009.

[13] J.J. Collins and I. Stewart. A group-theoretic approach to rings of coupled biological oscillators. *Biological cybernetics*, 71(2):95–103, 1994.

[14] W.M. Kier D. Trivedi, C.D. Rahn and I.D. Walker. Soft robotics: biological inspiration, state of the art, and future research. *Advanced Bionics and Biomechanics*, 5(2):99–117, 2008.

[15] A. C. de Pina Filho, M. S. Dutra, and L. S.C. Raptopoulos. Modeling of a bipedal robot using mutually coupled rayleigh oscillators. *Biological cybernetics*, 92(1):1–7, 2005.

[16] A. C. de Pina Filho, M. S. Dutra, and L. S.C. Raptopoulos. Modeling of a bipedal robot using mutually coupled rayleigh oscillators. *Biological cybernetics*, 92(1):1–7, 2005.

[17] S. Degallier, C. P. Santos, L. Righetti, and A. Ijspeert. Movement generation using dynamical systems: a humanoid robot performing a drumming task. In *Humanoid Robots, 2006 6th IEEE-RAS International Conference on*, pages 512–517. IEEE, 2006.

[18] T. Flash and B. Hochner. Motor primitives in vertebrates and invertebrates. *Current Opinion in Neurobiology*, 15:660666, 2005.

[19] G. Fiorito T. Flash G. Sumbre, Y. Gutfreund and B. Hochner. Control of octopus arm extension by a peripheral motor program. *Science 293*, page 1845, 2001.

[20] C. D. Godsil, G. Royle, and C.D. Godsil. *Algebraic graph theory*, volume 8. Springer New York, 2001.

[21] M. Golubitsky, I. Stewart, P.-L. Buono, and J.J. Collins. Symmetry in locomotor central pattern generators and animal gaits. *Nature*, 401(6754):693–695, 1999.

[22] P. Graziadei. Muscle receptors in cephalopods. *Proc. R. Soc. Lond*, 161(B):392402, 1965.

[23] J.Y. Guan. Design and control strategy of a flexible, hyper-redundant robotic arm using electroactive dielectric polymers, 2012.

[24] N. G. Hatsopoulos. Coupling the neural and physical dynamics in rhythmic movements. *Neural Computation*, 8(3):567–581, 1996.

[25] A. L. Hodgkin and A. F. Huxley. A quantitative description of membrane current and its application to conduction and excitation in nerve. *The Journal of physiology*, 117(4):500, 1952.

[26] I. W. Hunter and S. Lafontaine. A comparison of muscle with artificial actuators. In *Solid-State Sensor and Actuator Workshop, 1992. 5th Technical Digest., IEEE*, pages 178–185. IEEE, 1992.

[27] A. J. Ijspeert. 2008 special issue: Central pattern generators for locomotion control in animals and robots: A review. *Neural Networks*, 21(4):642–653, 2008.

[28] A. J. Ijspeert, A. Crespi, D. Ryczko, and J.-M. Cabelguen. From swimming to walking with a salamander robot driven by a spinal cord model. *Science*, 315(5817):1416–1420, 2007.

[29] T. Kanamaru. Van der pol oscillator. *Scholarpedia*, 2(1):2202, 2007.

[30] W. Kier and M.P. Stella. The arrangement and function of octopus arm musculature and connective tissue. *Journal of Morphology*, 268:831–843, 2007.

[31] W. M. Kier and M. P. Stella. The arrangement and function of octopus arm musculature and connective tissue. *Journal of Morphology*, 268(10):831–843, 2007.

[32] M. Kiyotoshi. Sustained oscillations generated by mutually inhibiting neurons with adaptation. *Biol. Cybern.*, 52(3):367–376, 1985.

[33] G. Kofod and P. Somrner-Larsen. Some aspects of large strain actuation in dielectric elastomers. In *Electrets, 2005. ISE-12. 2005 12th International Symposium on*, pages 208–211. IEEE, 2005.

[34] G. Kovacs, L. Düring, S. Michel, and G. Terrasi. Stacked dielectric elastomer actuator for tensile force transmission. *Sensors and Actuators A: Physical*, 155(2):299–307, 2009.

[35] W. Lai, A. F. Bastawros, and W. Hong. Out-of-plane motion of a planar dielectric elastomer actuator with distributed stiffeners. In *SPIE Smart Structures and Materials+ Nondestructive Evaluation and Health Monitoring*, pages 834011–834011. International Society for Optics and Photonics, 2012.

[36] P. Lochmatter. *Development of a Shell-like Electroactive Polymer (EAP) Actuator*. PhD thesis, 2007.

[37] D. R. McMillen, G. M.T. DEleuterio, and J. R. P. Halperin. Simple central pattern generator model using phasic analog neurons. *Physical Review E*, 59(6):6994, 1999.

[38] S. Mondal, A. Nandy, P. Chakraborty, and G.C. Nandi. A central pattern generator based nonlinear controller to simulate biped locomotion with a stable human gait oscillation. *International Journal of Robotics and Automation (IJRA)*, 2(2):93–106, 2011.

[39] G.C. Nandi, A. Ijspeert, and A. Nandi. Biologically inspired cpg based above knee active prosthesis. In *Intelligent Robots and Systems, 2008. IROS 2008. IEEE/RSJ International Conference on*, pages 2368–2373. IEEE, 2008.

[40] R. Olfati-Saber and R. M. Murray. Consensus problems in networks of agents with switching topology and time-delays. *Automatic Control, IEEE Transactions on*, 49(9):1520–1533, 2004.

[41] Ron Pelrine, Roy Kornbluh, Qibing Pei, and Jose Joseph. High-speed electrically actuated elastomers with strain greater than 100%. *Science*, 287(5454):836–839, 2000.

[42] Q.-C. Pham and J.-J. Slotine. Stable concurrent synchronization in dynamic system networks. *Neural Networks*, 20(1):62–77, 2007.

[43] J.-S. Plante and S. Dubowsky. On the nature of dielectric elastomer actuators and its implications for their design. In *Smart Structures and Materials*, pages 61681J–61681J. International Society for Optics and Photonics, 2006.

[44] L. Righetti and A. J. Ijspeert. Programmable central pattern generators: an application to biped locomotion control. In *Robotics and Automation, 2006. ICRA 2006. Proceedings 2006 IEEE International Conference on*, pages 1585–1590. IEEE, 2006.

[45] K. Seo, S.-J. Chung, and J.-J. E. Slotine. Cpg-based control of a turtle-like underwater vehicle. *Autonomous Robots*, 28(3):247–269, 2010.

[46] K. Seo and J.-J. Slotine. Models for global synchronization in cpg-based locomotion. In *Robotics and Automation, 2007 IEEE International Conference on*, pages 281–286. IEEE, 2007.

[47] M. Sfakiotakis, A. Kazakidi, N. Pateromichelakis, J. A. Ekaterinaris, and D. P. Tsakiris. Robotic underwater propulsion inspired by the octopus multi-arm swimming. In *Robotics and Automation (ICRA), 2012 IEEE International Conference on*, pages 3833–3839. IEEE, 2012.

[48] G. Sumbre, G. Fiorito, T. Flash, and B. Hochner. Octopuses use a human-like strategy to control precise point-to-point arm movements. *Current biology*, 16(8):767–772, 2006.

[49] V. Vavourakis, D. Bampasakis, A. Kazakidi, N. Pateromichelakis, J. A. Ekaterinaris, and D. P. Tsakiris. Generation of primitive behaviors for non-linear hyperelastic octopus-inspired robotic arm. In *Biomedical Robotics and Biomechatronics (BioRob), 2012 4th IEEE RAS & EMBS International Conference on*, pages 725–730. IEEE, 2012.

[50] T. Flash Y. Gutfreund, H. Matzner and B. Hochner. patterns of motor activity in the isolated nerve cord of the octopus arm. *Biol. Bull.*, 211:212–222, 2006.

[51] B. Hochner Y. Yekutieli, Roni Sagiv-Zohar and T. Flash. Dynamic model of the octopus arm. i. biomechanics of the octopus reaching movement. *Journal of Neurophysiology*, 94:1443–1458, 2005.

[52] B. Hochner Y. Yekutieli, Roni Sagiv-Zohar and T. Flash. Dynamic model of the octopus arm. (ii). control of reaching movements. *Journal of Neurophysiology*, 94:1459–1468, 2005.

[53] Y. Yekutieli, R. Mitelman, B. Hochner, and T. Flash. Analyzing octopus movements using three-dimensional reconstruction. *Journal of neurophysiology*, 98(3):1775–1790, 2007.

[54] Y. Yekutieli, G. Sumbre, T. Flash, and B. Hochner. How to move with no rigid skeleton? *Biologist*, 49(6):250–254, 2002.

[55] C. Zhou and K. H. Low. Design and locomotion control of a biomimetic underwater vehicle with fin propulsion. *Mechatronics, IEEE/ASME Transactions on*, 17(1):25–35, 2012.